SMART TWISTING ACTIVE ROTOR (STAR) – PRETEST PREDICTIONS

Berend G. van der Wall, berend.vanderwall@dlr.de, DLR (Germany)
Joon W. Lim, joon.w.lim.civ@army.mil, US Army DEVCOM AvMC (USA)
Johannes Riemenschneider, johannes.riemenschneider@dlr.de, DLR (Germany)
Steffen Kalow, steffen.kalow@dlr.de, DLR (Germany)
Gunther A. Wilke, gunther.wilke@dlr.de, DLR (Germany)
D. Douglas Boyd, Jr., d.d.boyd@nasa.gov, NASA (USA)
Joelle Bailly, joelle.zibi@onera.fr, ONERA (France)
Yves Delrieux, yves.delrieux@onera.fr, ONERA (France)
Italo Cafarelli, italo.cafarelli@onera.fr, ONERA (France)
Yasutada Tanabe, tan@chofu.jaxa.jp, JAXA (Japan)
Hideaki Sugawara, sugawara.hideaki@jaxa.jp, JAXA (Japan)
Sung N. Jung, snjung@konkuk.ac.kr, Konkuk University (Korea)
Seong H. Hong, shsky0721@konkuk.ac.kr, Konkuk University (Korea)
Do-Hyung Kim, dhkim@kari.re.kr, KARI (Korea)
Hee J. Kang, hkang@kari.re.kr, KARI (Korea)
George Barakos, george.barakos@glasgow.ac.uk, Glasgow University (UK)
Rinaldo Steininger, 2238057S@student.gla.ac.uk, Glasgow University (UK)

Abstract

A Mach-scaled model rotor with active twist capability is in preparation for a wind tunnel test in the large low-speed facility (LLF) of the German-Dutch wind tunnel (DNW) with international participation by DLR, US Army, NASA, ONERA, KARI, Konkuk University, JAXA, Glasgow University and DNW. To get the maximum benefit from the test and the most valuable data within the available test time, the tentative test matrix was covered by predictions of the partners, active twist benefits were evaluated, and support was provided to the test team to focus on the key operational conditions.

1. INTRODUCTION

After World War II, helicopters were increasingly introduced into many specialized operations that could not be served by fixed-wing aircraft. Today, these operations include service for offshore, commercial, civil, military applications, search and rescue, and many others. Helicopters combine the generation of lift and propulsive force in one main element: the main rotor with several blades revolving around the hub. The aerodynamic environment of rotating blades in forwards flight inherently generates a large bandwidth of unsteady aerodynamic forces and moments acting on them. Their dynamic response depends on their flexibility, dynamic characteristics, and on the type of attachment to the hub. It includes motions in all their degrees of freedom: rigid and elastic blade flap, lag, and torsional motion. Centrifugal forces acting on the rotating blades in motion further introduce steady and dynamic loads and inertia couplings between the various blade degrees of freedom.

In steady flight, all these unsteady blade aerodynamic and inertial forces and moments are repetitive each revolution and thus can be represented as integer multiples, n, (so-called harmonics) of the rotor fundamental rotational frequency, Ω. At the rotor hub, the forces and moments introduced by all the blades are additive and are transmitted via the rotor shaft to the fuselage of the helicopter. This superposition of a wide range of harmonic loads at the hub and the transformation into the nonrotating helicopter frame results in vibratory forces and moments that consist

of integer multiples, m, of the fundamental frequency, Ω, times the number of blades, N_b[1],[2].

Depending on the operational condition, the blade tip vortices trailed into the rotor wake form a spiral that can be close to all blades of the rotor. This happens especially during landing approach in descending flight, when the rotor inflow due to flight speed is oriented upwards and is of the same order as the thrust-induced inflow. Blade-vortex interactions (BVI) develop in a large variety of geometries with respect to the individual's vortex axis orientation relative to the interacting blade's leading-edge orientation in space. The phenomenon when the blade leading edge and the vortex axis are parallel with very little vertical distance between them is of special interest. This generates fast and strong modifications of the blade surface pressure distributions[3]. These rapid modifications to surface pressure happen when vortices – with their high swirl velocities and small vortex core dimensions (significantly smaller than the blade chord length) – pass the blade quickly. Consequently, strong impulsive noise is radiated, especially downwards.

Compared to fixed-wing aircraft, the helicopter vibration levels are much higher. They affect the crew and passengers adversely and reduce the lifetime of mechanical components. The noise radiation especially during landing approach near the ground is a concern for the outside environment and is also a certification issue of helicopters. Because of the above, both vibration and noise reduction have been a major issue since helicopters entered service. Because the rotor vibratory forces and moments are functions of the rotor harmonics and the number of blades, only a few rotor blade harmonics need to be controlled to reduce or eliminate vibration. Active rotor control has thus been under investigation since the 1950s, mostly by means of higher harmonic control (HHC) systems[4]. These are comprised of actuators underneath the swashplate and introduce the harmonics n = N_b − 1, N_b, N_b + 1 to the rotor blade by proper phasing of the actuator motion. These actuator controls are superimposed on the pilot's controls, which also move the swashplate.

The advantage of these HHC systems is that all components are in the nonrotating frame of the fuselage and, with respect to certification and safety of operation, can easily be made redundant. A disadvantage to the HHC systems is that many masses (e.g. push-rods underneath the swashplate, the swashplate itself, the pitch link push rods, all the blade attachment, and all the inner part of the blades) need to be moved with high frequency. Moving masses in this manner requires a large amount of power and makes the system heavy. Another disadvantage is the limited number of harmonics that can be transmitted to the rotor blades by the kinematics of the swashplate. This type of HHC system is only effective for rotors with more than 3 blades, which is currently most helicopters with a gross weight of more than two tons.

Numerical investigations have shown that a blade control of twice per revolution (2p, or n = 2) might be beneficial for rotor power reduction in fast forwards flight, and it was beneficial for reducing BVI noise in low speed descent flight. To overcome the disadvantages of HHC systems, individual blade control (IBC) systems with actuators at or in every individual rotor blade were investigated soon after the HHC systems were examined[5]. These IBC systems are comprised of actuators above the swashplate, for example replacing the pitch link push rods. Still, the blade root attachments and inner part of the blade must be moved with high frequency. However, IBC systems can control any frequency on all blades, and can also have different controls between the blades (if needed, for example, for in-flight blade tracking).

On-blade controls like trailing edge flaps are also considered IBC systems, with the further advantage that trailing edge flaps move only a very small device at the location where it is most effective, thus requiring significantly less power than a blade root control system. The disadvantage of IBC systems is that they all need power (often hydraulic) and signal transmission between the nonrotating and the rotating frame. Such a system is difficult to make redundant for safety and is therefore a major certification issue. In addition, these systems have mechanical components moving under large centrifugal forces that often were found biasing the controls significantly.

Recently, an IBC system capable of controlling every blade individually with all actuations still underneath the rotor was invented by DLR. This system comprised a multiple-swashplate control such that, for up to 3 blades of a rotor, one swashplate needs to be installed. For example, rotors with 1-3 blades require one swashplate; rotors with 4-6 blades require two independent swashplates; and rotors with 7-9 blades require three independent swashplates. It was tested successfully with a 4-bladed rotor[6] and a 5-bladed rotor[7] in the DNW-LLF. The advantages of that

system are that the entire system is in the nonrotating frame, all IBC capabilities are achieved, and redundancy can be obtained. The disadvantages are that the weight penalty and mechanical complexity grow with several swashplates instead of one, and three actuators per swashplate are required.

To avoid many of the disadvantages of IBC systems, active twist control of helicopter rotor blades was initiated around 1990 using smart materials as actuators. Several survey papers showing different applications of these materials were published in recent years[8]-[13]. One of the concepts, active twist of rotor blades, appears most promising because it twists the blade by introducing torsional moments along its span. Active twist is introduced by macrofiber composite (MFC) actuators embedded in the skin of rotor blades that are based on piezoceramic materials. These MFC actuators can expand or contract, even at high frequencies, when a voltage is applied across them. Distributed and oriented appropriately on the upper and lower surface of the blade, they can act as a sort of artificial muscle, which can elastically twist the entire blade by introducing torsional moments all along the actuated region.

Such a system was first demonstrated by the NASA/Army/MIT Active Twist Rotor (ATR) project[14]-[21]. The advantages of active twist systems are that no mechanical parts are present, only the aerodynamic active parts of the rotor blade are actuated, and the airfoils remain unchanged. The disadvantages are that electric energy must be transmitted into the rotating frame, no redundancy of actuators is easily possible, and the MFC actuator material increases the blade weight. The ATR was successfully tested in the heavy gas, variable density test medium of the NASA Langley Transonic Dynamics Tunnel by means of an aeroelastically scaled, four-bladed model rotor of 1.4 m radius, 0.107 m chord, -10° pretwist, a tip Mach number of 0.6, and a relatively high natural frequency of torsion above 7p. Hovering tests were performed in 1999 in the closed test section[16] evaluating the active twist performance with respect to statically and dynamically twisting the blade, and tests with wind followed in 2000 mainly for investigation of vibration reduction by means of active twist control[17],[18].

Advance ratios from 0.14 (with a shaft angle sweep) to 0.367 (level flight) were executed without actuation (baseline) and with active twist control using 3p, 4p, and 5p, respectively. Fixed-frame vibratory loads could be reduced by 60-95%, and 3p control was found most effective, confirming results of many HHC and IBC tests performed before[4],[5]. The actuators were spanning from 30 to 98% radius and were able to introduce up to 1.4° twist amplitude with 1000 V amplitude input at each of the control frequencies. Because of the very high blade natural frequency in torsion, the control frequencies used could not make use of torsional amplification that might have been possible if the blade natural frequency had been closer to the active twist control frequencies.

In the early 1990s, DLR started active twist rotor investigations, initially focusing on extension-torsion coupling based on a discrete actuator in the blade tip region[22]. Later examinations used the skin-embedded MFC actuator concept like the ATR. After several prototypes were built and whirl-tower tested, the Smart Twisting Active Rotor (STAR) project originated in 2007[23],[24]. The goals were to build and test a large highly instrumented Mach-scaled model rotor with active twist capability for investigation of vibration, noise, and power reduction and to compare results to HHC and IBC tests performed previously. After individual bench tests with each blade[25], the effort progressed to a test with all four blades on DLR's rotor test rig in 2013[26]. Predictions were performed for the test matrix, clarifying the possible benefits of active twist[27]-[29].

However, the test with all four blades on the rotor test rig revealed strains that were too large for the actuators, resulting in many local cracks in the actuators and in overloading of the high voltage amplifiers. These issues finally led to cancellation of the subsequently planned DNW-LLF test. After the redesign of the blade, the overall strains were reduced to a level that the actuators could carry without the previous types of actuator failures. This redesign was demonstrated with a prototype blade using a long-term whirl tower test under actuation[30]-[32]. A fully instrumented STAR set of redesigned rotor blades was built again and the individual blade whirl tower tests took place in the spring of 2022, followed by the pretest of the full rotor on the rotor test rig. From 2005 until present, the STAR activities were performed within an international team comprising DLR, NASA, US Army, ONERA, Konkuk University, KARI, JAXA, DNW and recently University of Glasgow. A new DNW test is planned for 2023 and prediction activities were again performed by all with the new blade design.

2. STAR ROTOR BLADE

The blade geometry and airfoil of the STAR rotor are like the Bo105, but they are arranged in an articulated hub and rotate clockwise when looking at the rotor from above. The load-bearing structure of the blades consists of a carbon fiber reinforced polymer (CFRP) main spar fitted with balance weights in the nose area and CFRP straps near the trailing edge. To generate the active twist, 30 actuators have been integrated into the two-layer glass fiber reinforced polymer (GFRP) skin of each rotor blade.

Numerous strain gauges measure the strains in the flap and lead-lag bending and tension directions. To measure the aerodynamic pressure distribution around the airfoil, a total of more than 200 pressure sensors is installed in the five STAR blades, Figure 1. Detailed information regarding the structure of the blades and the complex manufacturing process is described in Kalow et al.[31]
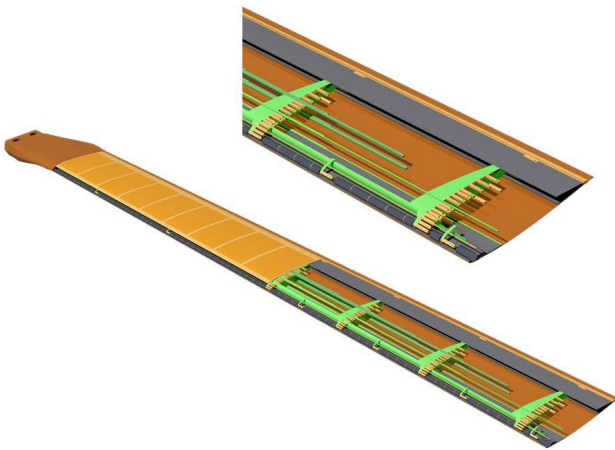

Figure 1: Detailed rotor blade design.

The final blades were investigated for blade stiffness and location of the elastic axis in a specialized test stand shown in Figure 2. This test stand enables the rotor blade in vertical alignment and clamped at the root to be loaded with forces in the bending direction at different chordwise positions. A dedicated displacement measurement using a digital image correlation (DIC) system allows correlation between forces and displacements, which allows for the determination of the blade stiffnesses.

Figure 3 shows the blade properties of the five rotor blades in comparison to the average of all experimentally determined blade properties. These mainly show the similarity of all the blades within 5% of the average, which is an essential element for the operation in the wind tunnel. Another important point is that the performance of the actuators is very similar in all

blades and is already sufficient to achieve a twist of at least $\pm 2°$ that is required for all operating conditions and for all test goals of the test matrix.

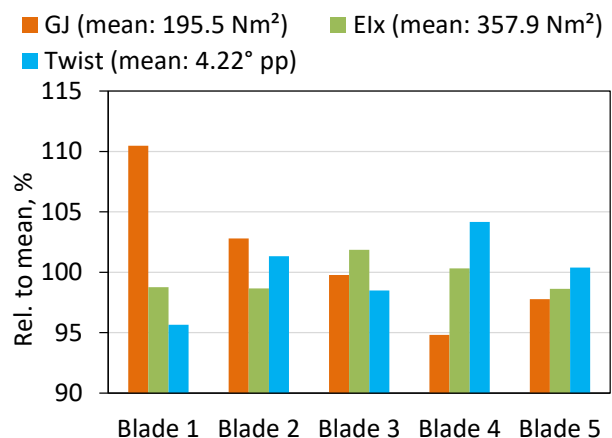Figure 2: Laboratory testing of blade stiffness.

Figure 3: Comparison of experimental STAR blade properties (deviation from averages given above).

Another important parameter for the blade-to-blade similarity is the built-in twist. To check this, a 3D scan of each blade was carried out. The analysis in Figure 4 shows, that the desired linear twist of -8° over the blade span was achieved for all blades.

Following the lab tests, the individual blades were installed in the DLR whirl tower for integrity testing as well as actuation testing under centrifugal loads. Figure 5 shows this whirl tower with an installed rotor blade. For individual blade testing, a counterweight was used for balancing and the blade integrated strain gauges were monitored. However, most

important is the blade tip pitch measurement, which was determined by images of the blade tip using an external camera.
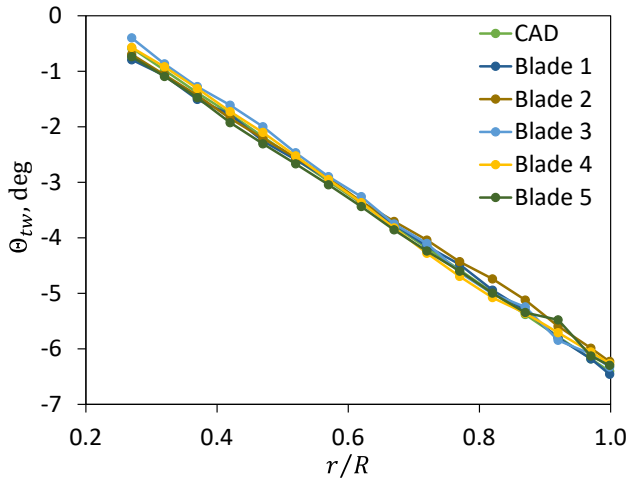

Figure 4: Measured twist distribution.

Figure 5: STAR blade in the whirl tower.

To reference the blade tip more clearly, two LEDs are installed in the tip plane at the leading and trailing edge, respectively. These optical measurements are examined in a real time LabVIEW analysis. Measurements are conducted for quasistatic excitation (0.15 Hz) as well as higher harmonics of 1p, 2p, 3p, 4p, and 5p of the nominal rotor speed.

These measurements serve as an additional check of the blade motion as well as system test for the actuators and the sensors installed. These sensors also serve as a risk reduction measure for the first rotor test with this setup as well as for the wind tunnel. The rotating hardware and the control software were also tested during these measurements. Components of the final control software running in LabVIEW were used.

3. TEST MATRIX AND CODES APPLIED

3.1. Test Matrix

The test matrix anticipated so far for the STAR rotor will be executed in the 6 m x 8 m open jet configuration of the DNW-LLF. It will cover the following operational conditions: reference baseline, BL, without actuation for measurement of the passive rotor; and with active twist for evaluation of its impact on the respective parameter(s) of interest.

The operational conditions are limited by the available motor power limit, maximum balance and component loads, and the wind tunnel speed range. The lower speed limit is defined by slipstream deflections caused by the rotor thrust and depends on the cross-sectional size of the model as well as on the presence or absence of the wind tunnel walls.

For the 6 m x 8 m open jet configuration chosen for this test, and using a nominal rotor thrust of 3600 N, the wind tunnel lower speed limit is estimated to be about $V_\infty = 20$ m/s. The maximum attainable wind speed is about $V_\infty = 78$ m/s. Within the test matrix, the minimum selected wind speed will be 22 m/s and the maximum 76 m/s, leading to blade tip speed ratios of $V_\infty/(\Omega R) = 0.1$ and 0.35, respectively, at 100% RPM and up to 0.7 at 50% RPM.

The test matrix is comprised of the following conditions:

- Hover at $V_\infty = 0$ m/s with a thrust sweep for evaluation of the Figure of Merit (FM). Steady active twist with a 0p harmonic applied for FM improvement.

- Level flight with $V_\infty = 22$ to 76 m/s wind speed and up to three different rotor loadings for code validation, passive rotor only.

- Flight path variation (γ-sweep) at 33 m/s with identification of the maximum BVI noise radiation condition. Application of 2p, 3p, 4p, and 5p active twist harmonics for evaluation of BVI noise reduction and vibration reduction.

- High load at 33 m/s investigating vortex-induced stall of the rotor at 50% nominal RPM. Active twist with a 2p harmonic for stall alleviation.

- High speed at 76 m/s with focus on power, vibration and high-speed impulsive (HSI) noise radiation. Active twist with 0p, 1p, and 2p harmonics for power, vibration and HSI noise reduction.

- High advance ratio of $\mu = 0.7$ at 50% RPM with a variation of the shaft angle (α_S-sweep). Application of 0p and 2p active twist harmonics at 0° and 180° phase for evaluation of its impact on power and vibrations. At $\alpha_S = 0°$, an active twist application with a 2p harmonic and a phase sweep.

For level flight and the flight path variation (moderate climb to steep descent), the rotor trim is performed for rotor lift (= scaled weight) and propulsive force (in wind axis) to overcome a virtual fuselage drag. Alternatively, a trim to their equivalent in the rotor shaft axis system can be performed, which is inclined such that the resultant of lift and propulsive force are in line with the shaft axis. Thus, the shaft axis force $F_z = T$ and $F_x = 0$ N. In either case, the hub rolling moment in the shaft axis system is trimmed to zero: $M_x = 0$ Nm.

The high load case condition with vortex-induced stall represents a high-g maneuver in cruise flight with a shaft angle fixed to $\alpha_S = 0°$ in the wind tunnel. Due to loads exceeding the balance limits at full RPM it is performed with half RPM and the hub moments are trimmed to zero. The high advance ratio condition represents a slowed rotor with half RPM at full wind speed of 76 m/s. A tip speed ratio of almost $\mu = 0.7$ is obtained. Here, the collective control angle is fixed to $\Theta_{75} = 4°$, a shaft angle sweep performed from $\alpha_S = -4°$ to +4°, and the rotor trimmed to zero hub rolling and pitching moments in the shaft axis system by means of the cyclic control angles.

Whenever active twist is employed, a retrim of the rotor to the desired operational condition is performed. In case of the high advance ratio (50% RPM) conditions with active twist, the thrust is also retrimmed to the value obtained by the passive rotor using the collective control angle.

Operational limits were computed using the DLR S4 comprehensive rotor code (described in the following section) covering all the passive rotor and active twist conditions. Figure 6 exemplarily shows the rotor power expected in the various conditions.

Wind speeds between 0 and 20 m/s cannot be run with nominal thrust due to excessive deflection of the airflow and associated wall corrections, and 76 m/s is

the maximum achievable wind speed in that test section with the rotor model in it. The rotor drive system has a power limit of $P_{max} = 190$ kW, limiting the hover condition (used to measure a Figure of Merit curve). All test conditions are in the available range of the wind tunnel and rotor test rig capabilities, hover is limited by the available motor power.
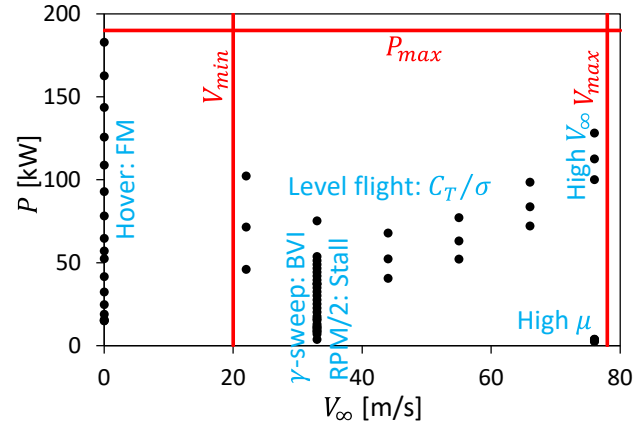

Figure 6: Power required for the test matrix conditions.

Hover testing is possible due to the absence of wind tunnel walls around the rotor, and its height of roughly 10 m above ground eliminates ground effect. However, the test hall – despite its huge dimensions – represents a volume closed on all sides such that some recirculation will develop, in proportion to the rotor thrust, that effectively generates an unavoidable slow vertical climbing condition. Pretest predictions ignore this recirculation effect until measured data are available and focus on the hover Figure of Merit (FM).

FM is defined by the ratio of ideal power (based on momentum theory) that is related to the total power consumed P_{tot}, Eq. (1), wherein T, ρ, A, R are the rotor thrust, air density, rotor disk area and the rotor radius, respectively.

$$\text{FM} = \frac{\sqrt{\frac{T^3}{2\rho A}}}{P_{tot}} \; ; \; A = \pi R^2 \tag{1}$$

Rotor vibration is measured by the rotor balance. The hub loads in the nonrotating frame (horizontal force F_x, lateral force F_y, vertical force F_z, rolling moment M_x, and pitching moment M_y) are analyzed for their 4p and 8p components. Following Crews[33], a vibration intrusion index, VI, is used as a nondimensional measure of vibration.

For computing VI, the ip hub forces $F_{x/y/z,i}$ are weighted by a factor of 0.5, 0.67, and 1, respectively,

and referenced to a virtual model-scale weight of $W_0 = 3600$ N, while the ip hub moments $M_{x/y,i}$ are referenced to RW_0, see Eq. (2).

$$VI = \sum_{i=4,8} \frac{\sqrt{\left(0.5F_{x,i}\right)^2 + \left(0.67F_{y,i}\right)^2 + (F_{z,i})^2}}{W_0}$$

$$+ \sum_{i=4,8} \frac{\sqrt{(M_{x,i})^2 + (M_{y,i})^2}}{RW_0}. \tag{2}$$

3.2. Rotor Codes Employed

The computations of the various conditions were performed by a variety of codes of different fidelity level, ranging from rotorcraft comprehensive analysis codes to coupled CFD/CSD approaches.

3.2.1. DLR-CA

The DLR comprehensive analysis tool, S4, is a high resolution, 4th generation comprehensive rotor simulation code[34],[35]. The finite-element-based structural dynamics modeling in S4 is based on Houbolt and Brooks equations[36]. The beam element has ten degrees of freedom. A semiempirical formulation of the airfoil coefficients based on the Leiss method[37] is used for unsteady blade motion, but further modification is made for the BVI problem. The fuselage interference flow effect is included at the blade sections using a semiempirically derived formulation from the potential theory[35].

The Mangler/Squire global wake model[38] is used for performance and vibration estimates, but an extended version of the Beddoes' prescribed wake geometry formulation[39] with multiple trailers is used for noise predictions, accounting for wake deflections due to harmonic rotor loading. Trim is performed with an azimuth increment of 1°, and the simulation uses the first six modes for a modal analysis. The noise radiation is computed using the acoustic code, APSIM[40], which is based on the Ffowcs Williams-Hawkings equations[41] and predicts the loading and thickness noise.

3.2.2. DLR-CFD

The DLR-CFD approach is based on the coupling of the DLR legacy flow solver FLOWer[42] with the comprehensive code, HOST[43] (Airbus Helicopters), used using the delta airloads approach[44]. On the structural side, the first eight eigenmodes are included. The inviscid fluxes are resolved using a 4th-order upwind scheme (SLAU2 with FCMT)[45]. The SA-DDES-

R[46],[47] turbulence model is applied for the computation of the eddy viscosity and transition is empirically predicted[48]. A dual time-stepping approach with a timestep equivalent to 1/4° of a revolution is used. The grid consists of 15 M grid points with a background grid spacing of $\Delta x/c = 0.17$ in the vicinity of the rotor and 1 M grid points for each blade grid. For the determination of the acoustics, the code APSIM[40] by DLR is used. For the high-speed flight condition, the porous formulation is used, whereas for the other flight conditions the surface formulation is applied.

3.2.3. ONERA-CA

Low to medium levels of fidelity are used at ONERA for aerodynamic and acoustic simulations. The low fidelity, finite-element-based HOST[43] comprehensive code developed by Airbus Helicopters solves for blade deformations. The aerodynamics model in HOST is based on a lifting line approach, for which the aerodynamic coefficients are directly interpolated using 2D semiempirical airfoil tables depending on the local sectional Mach number and the angle of attack. Theodorsen unsteady aerodynamics are used, and the corrections for yaw flow and stall are available. Different inflow models are used, depending on flight condition.

For the hover configuration, the finite state unsteady wake model (FiSuW) is used that expresses the induced velocity by means of Legendre polynomials for the radial distribution and Fourier series for the azimuthal variation[49]. For the High Advance Ratio cruise configuration, the prescribed helical wake code, METAR[50] is used iteratively within the trim loop. For the High Load cruise configuration, the fully time marching unsteady wake model, MINT[51], developed at ONERA is used. The wake is discretized in panels of constant gradient of potential jump, which improves the accuracy and the stability of the method compared to the model of the wake by vortex lattices. For the descent configuration, the full span free-wake model MESIR[52], developed at ONERA, computes the velocities induced by all trailed and shed vortex lattices using the Biot-Savart law.

The roll-up of the vortices is modelled through the MENTHE[53] code, which determines the intensities and radial locations of the vortices at the emission azimuths. Blade pressure distribution is then calculated by the unsteady singularity method ARHIS[54]. Finally, the noise computation is performed using the acoustic code PARIS[55], based on the Ffowcs Williams-

Hawkings equations[41]. It uses a time domain formulation and predicts the loading and thickness noise.

3.2.4. US, KU, KARI: CAMRAD II

The CAMRAD II comprehensive analysis code[56] was used by the US Army DEVCOM AvMC, the National Aeronautics and Space Administration (NASA), the Korea Aerospace Research Institute (KARI) and Konkuk University (KU). The structural model is based on a finite beam element formulation with each element having nine degrees of freedom. The number of finite elements used in this study ranges from 8 to 18 elements.

The section aerodynamics are based on the lifting line theory with C81 lookup table and ONERA EDLIN unsteady aerodynamic model is used. For the aerodynamics computation, 17 to 23 aerodynamic panels are used with a free wake analysis. The trim solution is obtained at 15° azimuth. For noise calculations, the aerodynamic response is recomputed at a higher resolution of 5°, 1.5° or 1° azimuth with the trim controls fixed (post trim). Noise calculation is performed using ANOPP2's Aeroacoustic Rotor Noise (AARON) tool[57] for the U.S. partners and an in-house code based on the Ffowcs Williams-Hawkings equations[41] for Korean partners.

3.2.5. KARI-CFD

The KARI CFD tool is the 3D unsteady viscous flow solver based on unstructured meshes, UMAP3D[58], coupled with CAMRAD II. The flow solver utilized a vertex-centered finite-volume scheme that is based on the Roe flux-difference splitting with an implicit time integration. The eddy viscosity is estimated by the Spalart-Allmaras one-equation turbulence model. The overset mesh technique and the mesh deformation technique using the spring analogy method were adopted to handle the relative motion and deformation of the rotor blades. The blade deformation was calculated by CAMRAD II, and the rotor trim was iteratively solved in CFD and CSD codes until it matched the trim target.

3.2.6. JAXA

The JAXA Computational Fluid Dynamics (CFD)/Computational Structural Dynamics (CSD) coupled tool consists of three computational codes for rotary wing application - rMode, rFlow3D, and rNoise that were developed in-house at JAXA. The rMode code computes the natural frequencies and mode shapes of the blade flap, lag and torsion modes that are based on Houbolt and Brooks equations[36].

The structured Navier-Stokes solver, rFlow3D, is based on a moving overset grid approach, and adopts a modified Simple Low-dissipative Advection Upstream Splitting Method (mSLAU) to adjust numerical dissipation by limiting the drag at very low Mach number[59]. SST-2003 turbulence model with $\gamma - Re_\Theta$ transition model[60] is applied for present predictions. Blade deformation is solved using the Ritz's modal decomposition method and then is loosely coupled with the CFD solver.

Rotor trim controls are iteratively solved in the CSD routine until matching with the trim targets. After a periodically converged solution is obtained, the rNoise code computes the noise generated by the rotor using Ffowcs Williams and Hawkings equations[41].

3.2.7. University of Glasgow (UofG)

The UofG in-house CFD/CSD framework HMB3 (Helicopter Multi-Block 3) is a finite volume solver on structured multiblock grids[61]. An overset grid method is used. HMB3 solves the Unsteady Reynolds Averaged Navier-Stokes (URANS) equations in integral form using the Arbitrary Lagrangian Eulerian (ALE) formulation for time-dependant domains, including moving boundaries. To evaluate the convective fluxes, the Osher[62] approximate Riemann solver is used, while the viscous terms are discretised using a 2nd-order central differencing spatial discretisation.

The MUSCL approach developed by van Leer[63], is used to provide high-order accuracy in space with the alternative form of the van Albada limiter[64] in regions of large gradients. The implicit, dual time-stepping method of Jameson[65] is employed. The linearized system of equations is solved using the Generalised Conjugate Gradient method with a BILU factorisation as a pre-conditioner[66]. From one-equation to four-equation turbulence models are available in HMB3 solver.

The 1994 $k - \omega$ SST model of Menter[67] is used in the predictions of the STAR rotor. The structural model solves for the linear scaling factors of the given number of precomputed eigenmodes as a function of time[68]. In steady simulations, time-independent beam or 3D-FEM analysis in MSC NASTRAN is coupled to CFD. Active twist can be applied via prescribed mesh rotation, or in MSC NASTRAN through a torsion moment in 1D-beams or through a thermal analogy method in 3D-FEM.

3.3. Further Information

3.3.1. Figure legend

Since many partners are involved in this project and the plots tend to have many lines, it was decided to place the legend of these graphs here to make them visible in the remainder of the paper, see Figure 7. Continuous lines represent CFD-based results, dashed lines pure comprehensive code results.
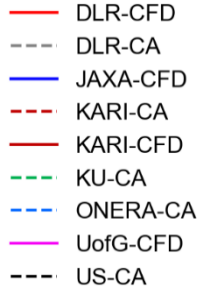
——	DLR-CFD
- - -	DLR-CA
——	JAXA-CFD
- - -	KARI-CA
——	KARI-CFD
- - -	KU-CA
- - -	ONERA-CA
——	UofG-CFD
- - -	US-CA

Figure 7: Universal line legend for the paper.

3.3.2. Active twist application

In the experiment, active twist is performed by application of steady (offset) and periodic voltage. The offset is needed due to the asymmetric voltage range of the actuators and amounts to 400 V, resulting in $M_{off} = 2.08$ Nm torsional moment along the actuated span of the blade. Including a safety margin, a dynamic range of 1000 V (5.2 Nm) relative to the offset could be used (= 100%), but only 50% (500 V; 2.6 Nm) and 80% (800 V, 4.16 Nm) will be used during dynamic actuation. In numerical simulations, the resulting torsional moments are applied by including a torsional moment couple near the inner and outer edges of the blade where the actuators end, for n = 0, 1, ..., 5:

$$M(\psi) = M_{off} + M_n cos(n\psi - \phi_n). \quad (3)$$

4. HOVER: FIGURE OF MERIT

Hover performance, together with the elastic deformations are predicted using high fidelity methods (CFD) and comprehensive analyses. The rotor figure of merit (FM) predictions by the 6 partners are shown in Figure 8. Acceptable agreements are obtained among these various prediction methods.

Elastic deformations with the change of blade loading are predicted with more scatter among the partners' results. The flap deformations predicted are almost agreeable among the partners as shown in Figure 9. However, large differences are observed in the tip torsional deformation as shown in Figure 10. Validation

with the experimental measurements of the blade deformations is expected after the test.

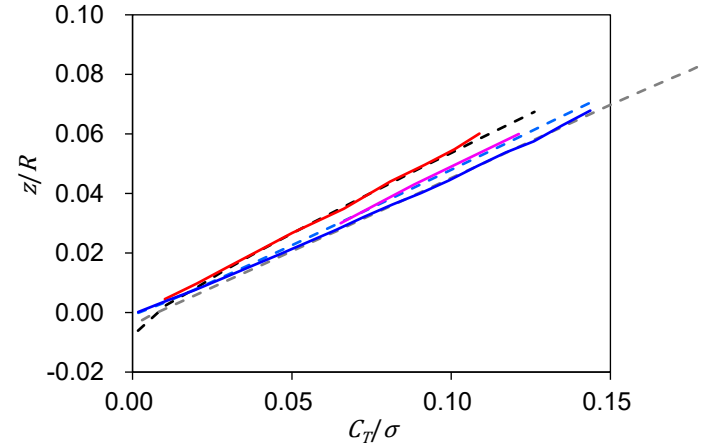Figure 8: Figure of Merit (FM) prediction.
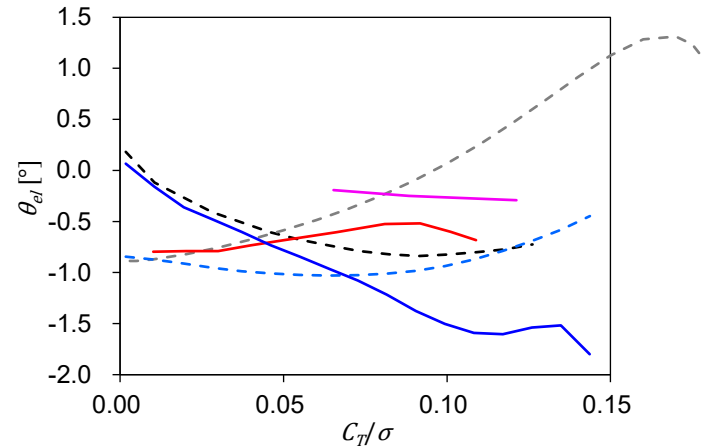

Figure 9: Flap deformation at the blade tip.

Figure 10: Torsion deformation at the blade tip.

The effect of static active twisting of the blade at nominal blade loading $C_T/\sigma = 0.064$ and 0.1 is examined by the partners. As shown in Figure 11, only 0.0007 to 0.007 of improvements of the FM are predicted when 80% of the full negative blade twist amplitude

with 400 V offset (actual static actuation of -400 V, negative voltage causes nose down twist) is applied.
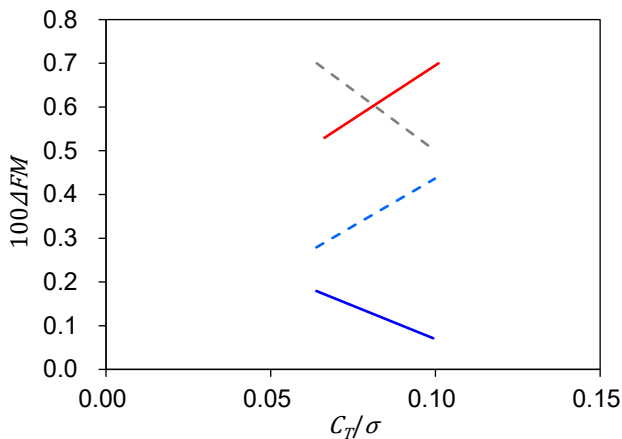

Figure 11: FM improvement with static actuation.

To further clarify the differences of aerodynamic modellings utilized by the partners, comparisons of the radial distributions of sectional normal force coefficient $C_n M^2$ for $C_T/\sigma = 0.064$ are shown in Figure 12. The distributions of $C_n M^2$ near the blade tip region remarkably change depending on the fidelity of the utilized prediction tool. The CFD results by DLR and JAXA showed an abrupt variation corresponding to formation of a tip vortex. The comprehensive tools utilizing tip loss modellings by DLR and ONERA show a simple decrease of aerodynamic loading towards the tip. The US team using a free-wake modelling shows an intermediate variation near the blade tip.

Figure 12: Radial distribution of sectional normal force for $C_T/\sigma = 0.064$.

Variation of the sectional pitching moment around the blade tip region is more sensitive to flow separation. As shown in Figure 13a, at the nominal target thrust condition of $C_T/\sigma = 0.064$, the pitching moment coefficient $C_m M^2$ shows a small decrease before increasing to a positive nose-up value near the blade tip as predicted by the CFD solvers. Such an abrupt change is not predicted by the comprehensive codes. When an obvious separation region forms at a large thrust condition of $C_T/\sigma = 0.144$, a sharp decrease of the pitching moment is observed, Figure 13b.
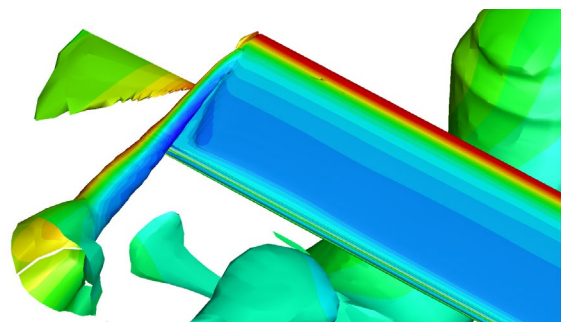

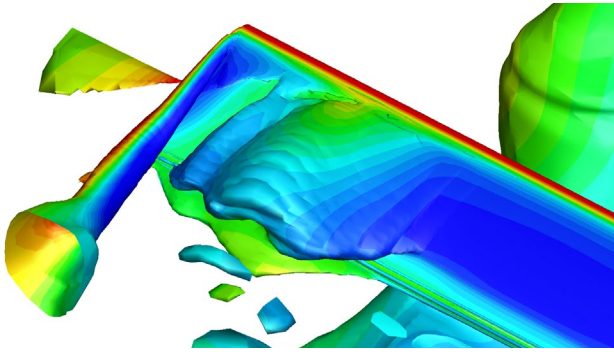(a) Pitching moment coefficient for $C_T/\sigma = 0.064$.

(b) Pitching moment coefficient for $C_T/\sigma = 0.144$.

Figure 13: Sectional pitching moment distributions.

The according flow fields computed by CFD are represented by the isosurface of Q-criterion in Figure 14. A local flow separation area is observed on the upper surface of the blade when $C_T/\sigma = 0.144$.

(b) Tip vortex for $C_T/\sigma = 0.144$.

Figure 14: Isosurfaces of Q-criterion around blade tip region (JAXA results).

5. DESCENT: BVI NOISE AND VIBRATION

It is desirable to assess the effect of active twist on Blade-Vortex Interaction (BVI) noise at a flight condition where BVI noise is a maximum. BVI noise here is defined as the unweighted, Overall Sound Pressure Level (OASPL) of the 6th through the 40th Blade Passage Frequency (BPF). The OASPL restricted to this frequency range is known as BVISPL. OASPL and BVISPL both have units of decibel (dB). The first step is to determine the flight condition on approach (flight path angle) at which BVI noise is a maximum. The flight path angle γ was varied from a 6° climb ($\alpha_S = -8.1°$ forwards shaft tilt) to a 12° descent ($\alpha_S = 9.9°$ aft shaft tilt).

Figure 15 shows a sample baseline (passive rotor, BL) computation for BVISPL on a horizontal plane, which is 1.1R below the rotor hub. The maximum BVISPL value is seen on the left side of the figure, which is the advancing side of the rotor. The US, KARI, ONERA, and DLR teams computed plots such as those seen in Figure 15 for the flight path angle variation described above. Each team extracted the maximum value of BVISPL from their predictions as a function of flight path angle. To compare the maximum BVISPL as a function of flight path angle from each partner, the largest of these maxima from each partner was subtracted from their respective results.

Figure 16 shows the change of noise level (ΔBVISPL) relative to the maximum BVISPL as a function of flight path angle γ for each partner. Positive values of γ are for climbing flight. Negative values of γ are for descending flight. These show that the predicted flight path angle where the highest BVISPL occurs is between approximately $-10°$ and $-7°$ descent angle. In

discussions with the partners, the decision was made to choose the 9° descending flight path angle ($\alpha_S = 6.89°$ aft shaft tilt) as the maximum BVISPL flight path angle. At this 9° descending flight path angle, active twist at frequencies equivalent to 2p, 3p, 4p, and 5p were applied, respectively. At each of the 2p, 3p, 4p, and 5p active twist frequencies, 50% and 80% of the maximum active twist amplitudes were applied at various azimuthal phases. The active twist is implemented as given in Eq. (3).
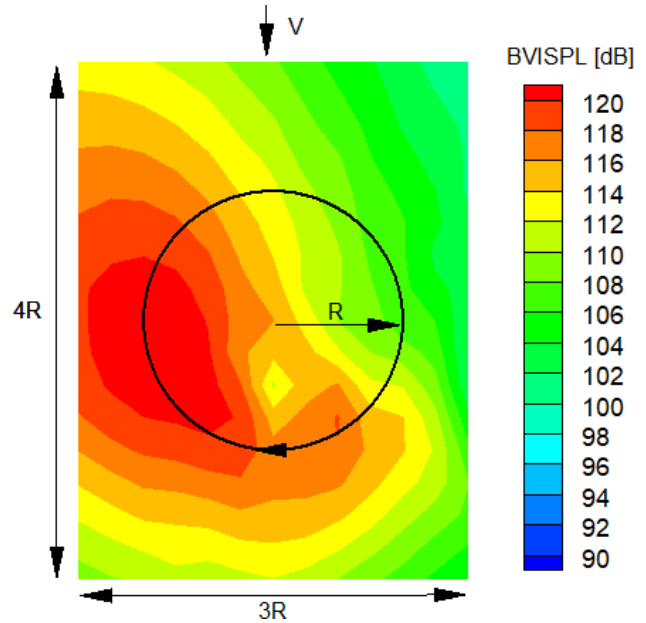

Figure 15: Sample BVISPL [dB] calculation on a plane 1.1R below the rotor for the BL case. The black circle represents the extent of the rotor disk.
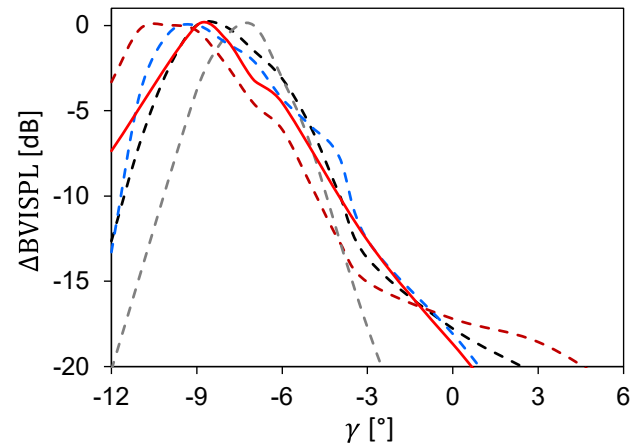

Figure 16: Change of noise level relative to its maximum as a function of the flight path angle.

The US team performed 2p, 3p, 4p, and 5p active twist computations at both the 50% and 80% activation amplitudes. The DLR-CA team performed computations for the same range of frequencies, but

acoustic post-processing was only performed for the most promising conditions at a few selective phase angles for the 2p, 3p, and 4p at the 50% activation amplitude. The KARI team performed computations for 2p, 3p, and 4p at the 80% activation amplitude. The ONERA team performed computations with 2p and 3p at the 50% activation amplitude.

Figure 17 shows predictions using 2p actuation at 50% and 80% amplitudes. The horizontal axis is the phase angle, φ, and the vertical axis is the change in BVISPL from the partners' respective maximum baseline BVISPL. There is a large variation of predicted results from the partners for the 2p actuation. A trend is that many of the phase angles have predicted ΔBVISPL to be near or less than zero. This tendency means that 2p should slightly reduce the maximum BVISPL at many phase angles. For individual partner's results, a preferred phase angle can be determined where BVISPL is reduced. However, when examining partners' results collectively, there is not a clear indication of a preferred amplitude or phase angle when using 2p active twist in this flight condition.
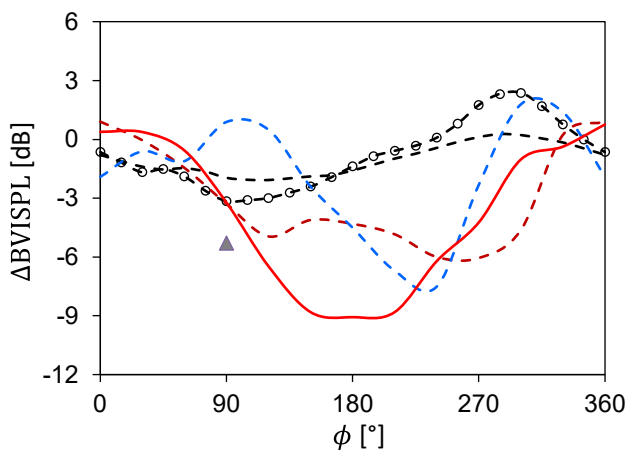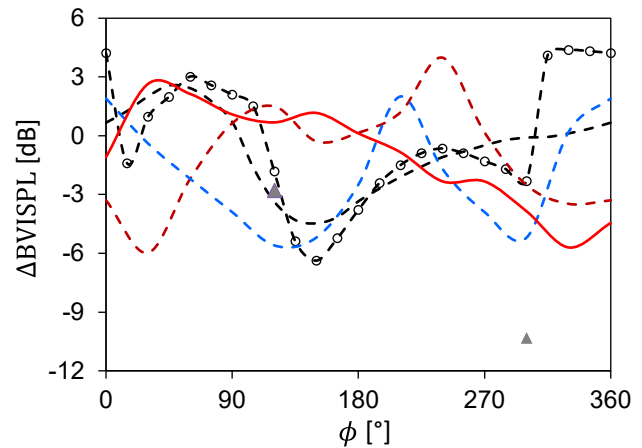

Figure 17: Change of noise level relative to its maximum as a function of 2p actuation with amplitudes of 50% and 80%. Dashed line with circles is the US 80% amplitude result. Triangle symbol is the result from DLR-CA.

Figure 18 shows predictions using 3p actuation at 50% and 80% amplitudes. The axis configuration is the same as that in Figure 17. Here, too, there is large variation of predicted results from the partners. Whereas the 2p predictions tended to be below (or sometimes slightly above) zero, in the 3p case, there appear just as many phases and amplitudes where the results are above and below the baseline maximum BVISPL. As with the 2p actuation, for individual partner's results for 3p actuation, a preferred phase

angle (or two) can be determined where BVISPL is reduced. However, when examining partners' results collectively, there is not a clear indication of a preferred amplitude or phase angle when using 3p active twist in this flight condition.

Figure 18: Change of noise level relative to its maximum as a function of 3p actuation with amplitudes of 50% and 80%. Dashed line with circles is the US 80% amplitude result. Triangle symbol is the result from DLR-CA.

Figure 19 shows predictions using 4p actuation at 50% and 80% amplitudes. In the 4p case there appear most phases and amplitudes where the results are above the baseline maximum BVISPL level. As such, 4p active twist actuation does not appear to be a good candidate for this flight condition.
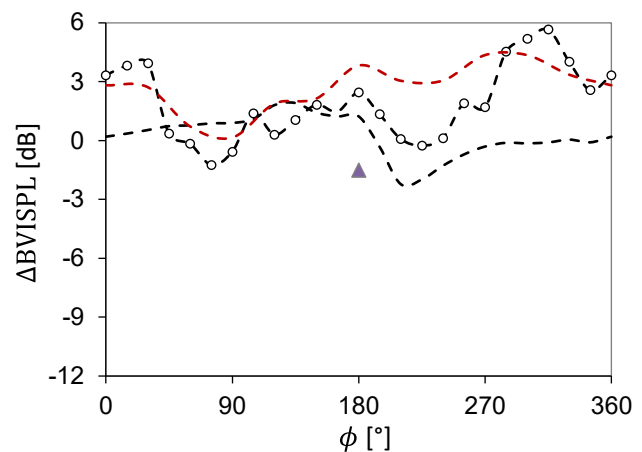

Figure 19: Change of noise level relative to its maximum as a function of 4p actuation with amplitudes of 50% and 80%. Dashed line with circles is the US 80% amplitude result. Triangle symbols are results from DLR-CA.

Figure 20 shows predictions using 5p actuation at 50% and 80% amplitudes. There is no clear trend that

indicates a preferred amplitude or phase of 5p actuation. These predictions, as anticipated, indicate that usage of 5p active twist will not be effective in reduction of the maximum BVISPL for this flight condition.
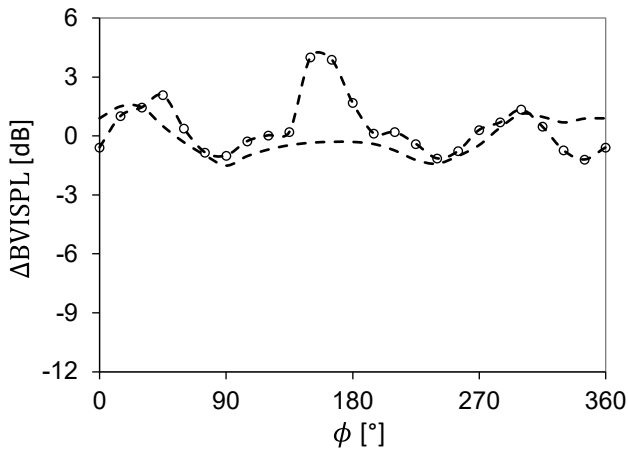

Figure 20: Change of noise level relative to its maximum as a function of 5p actuation with amplitudes of 50% and 80%. Dashed line with circles is the US 80% amplitude result.

6. HIGH SPEED: POWER, VIBRATION AND HSI NOISE

A moderate blade loading $C_T/\sigma = 0.0651$ level flight condition was chosen at high advance ratio $\mu = 0.349$ and $\alpha_S = -11.1°$ forwards shaft tilt. The compressibility effects and retreating blade stall lead to vibration and HSI noise. The goal of the active twist application in this flight condition is to reduce vibration, noise emission and rotor power.

The trim goal is a fixed thrust coefficient with zero rotor rolling and pitching moments. Aeroelastic rotor simulations were collected for the passive blade and for 2p with a control phase of 210° active twist of 50% amplitude. DLR-CFD, KARI and KARI-CFD, provided the 210° phase result, while US, DLR-CA and JAXA provided active twist phase sweeps in 30° increments. For the CFD results, KARI-CFD used a mesh of 28 M unstructured nodes, DLR-CFD up to 15 M structured cells, JAXA 15.8 M cells and UofG 36 M cells in total.

Due to the blade pitch increase caused by the offset voltage, the collective angles were lower by 0.2° to 1° between simulation results when compared to the baseline. The longitudinal cyclic required was decreased for the 90° and was increased for the 270° phase. The lateral cyclic of the phase sweeps were at their highest magnitude around 180°. JAXA predicted a power reduction with 210° active twist, while others

showed an equal or higher value than the baseline and showed increased power at other phases. The blade coning angle β_0 was increased slightly by active twist. The 210° phase produced a reduced Vibration Index (VI) compared to the passive rotor, but the scatter in VI is large, Figure 21. When accounting for the change in trim state when active twist is applied, most codes predicted a higher propulsive force. Calculating the L/D_e, all results apart from DLR show either a slight increase or small decrease, but DLR-CFD and S4 predict a large L/D_e improvement.
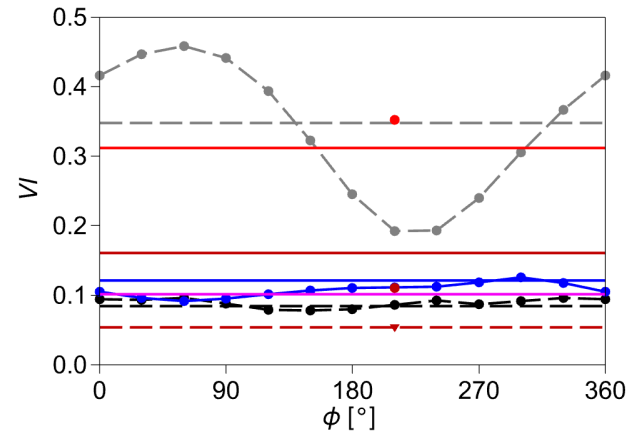

Figure 21: Vibration index results for baseline (horizontal line), 1p (DLR-CA only) and 2p actuation.

The L/D_e is shown in Figure 22. The DLR-CA result suggests that the voltage offset produced a linear change in required collective and a slightly lower L/D_e than baseline.
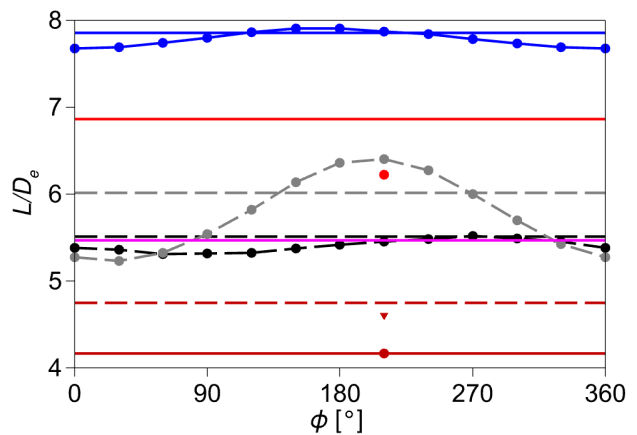

Figure 22: Lift to Drag-equivalent for baseline (horizontal lines), 1p (DLR-CA only) and 2p actuation.

The 1p active twist phase sweep directly impacted on the cyclic control angles and could affect vibration, flapping angles and show a small impact on L/D_e. The 2p phase sweep showed potential to reduce the vibration and increase L/D_e at the same phase, with

a direct impact on control angles and showed insignificant changes for blade flapping.

Normal and chordwise forces and sectional moments were recorded for three outboard blade locations. Strong code to code agreement was found. Figure 23 represents the normal force agreement for all radial sections, where DLR-CA and DLR-CFD shows higher loading peaks and offloading than other partners.
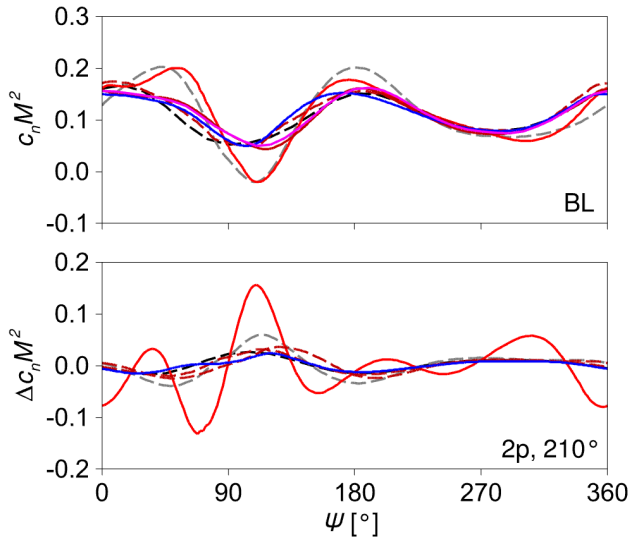

Figure 23: Normal force coefficient at $0.773R$. Difference to BL due to active twist below.

The chordwise force correlation is very strong, Figure 24. The active twist reduced the loading peaks and troughs at and outboard of this location, but it increased nonpeak loading. The code-to-code correlation was very strong for the chordwise force, and increased lift on the retreating side can be observed.
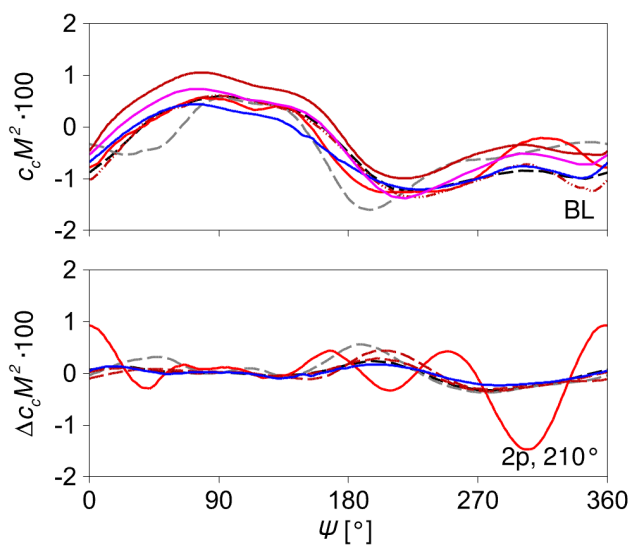

Figure 24: Chordwise force coefficient at $0.773R$. Difference to BL due to active twist below.

Figure 25 shows how active twist reduces the pitch-down tip moment in the second quadrant of the rotor disk. There is some small spread among the results on the advancing half of the rotor disk.
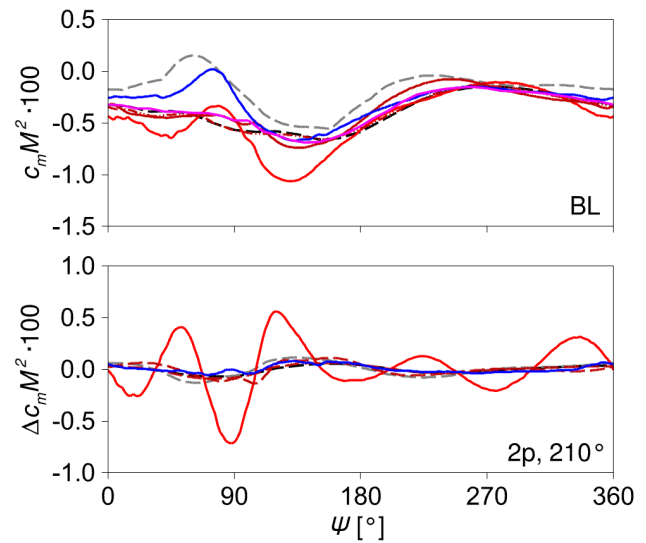

Figure 25: Sectional moment coefficient at $0.773R$. Difference to BL due to active twist below.

The provided values of elastic blade tip torsion in Figure 26 did not fully match the good correlations of the aerodynamic forces. DLR-CFD predicts the largest pitch-down tip twist at the advancing side. There is a clear trend towards a reduction at the advancing side for all partners when active twist was applied, and the retreating blade tip was pitched higher than in the baseline case.
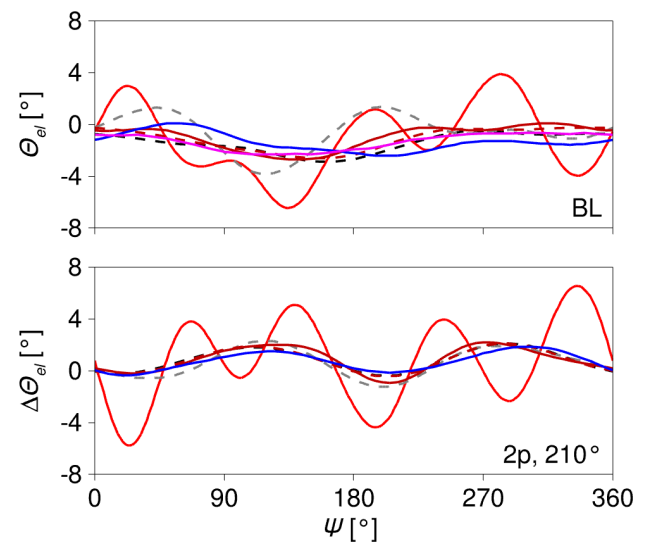

Figure 26: Blade tip elastic torsion. Difference to BL due to active twist below.

HSI noise radiation in the horizontal plane 1.1R below the rotor is shown in Figure 27. The peak noise level

was recorded to be ahead of the advancing rotor blade, at a level slightly below the tip path plane on a 1.5R sphere. The sound pressure level (SPL) did not vary significantly from 124 to 125 dB SPL of the passive rotor, when the 2p active twist was applied with a phase of 210°. The SPL obtained by JAXA for the passive rotor, 2p 180° (min. noise) and 2p 330° (max. noise), showing a potential to reduce noise.
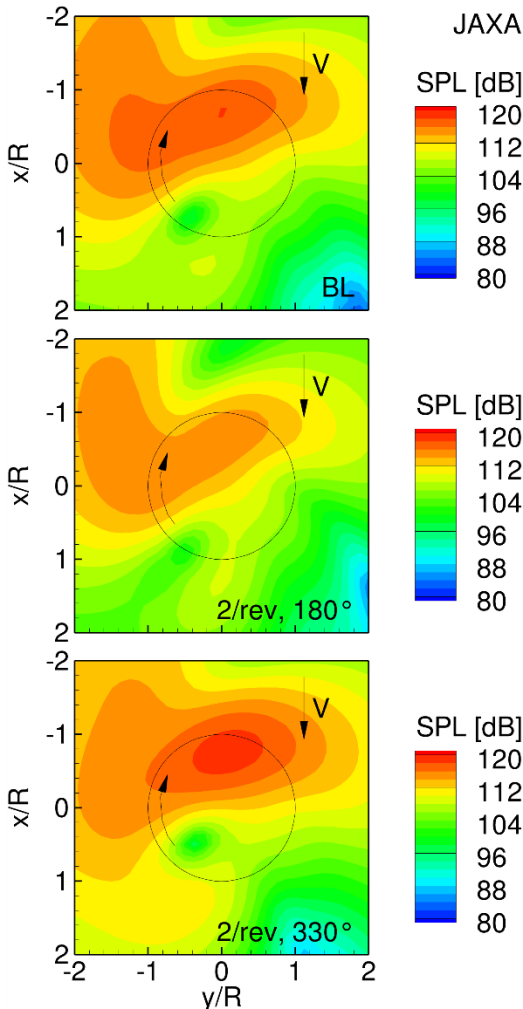

Figure 27: Noise level results of JAXA code in the horizontal plane 1.1R below the rotor hub for baseline (BL), minimum (2p, 180°) and maximum noise (330°).

With the trim goal of zero pitching and rolling moments, the propulsive force of the rotor was unconstrained. This did not allow a direct rotor power comparison, but the Lift to Drag ratio was compared. The 2p active twist at 210° phase angle showed a benefit in vibration index and L/D_e for most codes.

Force correlations were matching well, and the offsets produced by the active twist were consistent among codes. The blade elastic deformations have some differences, which shall be addressed in future

computations. The impact of the chosen active twist on the peak rotor noise direction was marginal. The blade sections chosen are coincident with the location of pressure sensors to be validated at the experiment. It is recommended to inspect the effect of the twist offset voltage and 1p in addition to 2p in the experiment, to isolate the individual contributions. Microphones ahead of and below the rotor disk are recommended to capture the noise peaks.

7. HIGH LOAD: VORTEX-INDUCED STALL

The goal of this test condition is to investigate the dynamic stall phenomenon caused by the upwash of the preceding blade-tip vortex on the rotor's retreating side. The potential to reduce the stall through active twist actuation will be explored. This flight condition occurs for a regular helicopter when highly loaded, for example during manoeuvering flight. That condition is therefore representative for the boundary of the operational envelope of a regular helicopter rotor.

The difficulty in mimicking this flight condition is that it is usually associated with a dynamic behavior such a pull-up maneuver, which would be too difficult to replicate in the wind tunnel. For the general topic of dynamic stall, we refer the avid reader to the recent overview papers by Smith[69] and by Castells[70].

Initially, it was attempted to operate the rotor at nominal RPM and an advance ratio of $\mu = 0.3$ in combination with a propulsive force trim, where the thrust would be gradually raised. However, multiple issues were encountered on this first attempt: First, the maximum thrust required to achieve a measurable stall was close to the limit of the rotor balance. Second, the power required was also close to the maximum power output of the motor. Additionally, a few partners predicted a strong aeroelastic coupling effect for the blade torsion exciting the second torsion eigenmode.

Thus, the flight condition has been altered to operate at half the nominal rotor RPM and wind tunnel speed to bring down the overall aerodynamic forces and moments. This roughly reduces the forces by a factor of 4 and reduces the required power by a factor of 8, therefore leaving an ample margin in power as well as scale limits. The loss of Mach scaling is considered acceptable because it is mostly a concern for the advancing blade side, where the phenomenon of interest does not occur. Additionally, the propulsive force trim is changed to a zero-moments trim at zero shaft tilt $\alpha_S = 0°$. In the first phase of this test case, the

thrust is varied to find a common data point where most partners observe a stall. In the second phase, the actuation is applied for this common data point.

In Figure 28, the control angles obtained by each partner for different blade loadings are reported. The simulations were run up to the maximum achievable thrust. Especially for the lower thrusts, a good agreement is observed, but with increasing thrust the results partially diverge. For example, the JAXA-CFD results predict a stronger rise in the magnitude of the control angles than the ONERA-CA results. Both of these partners can converge their trim solutions at notably higher thrusts than the other partners.
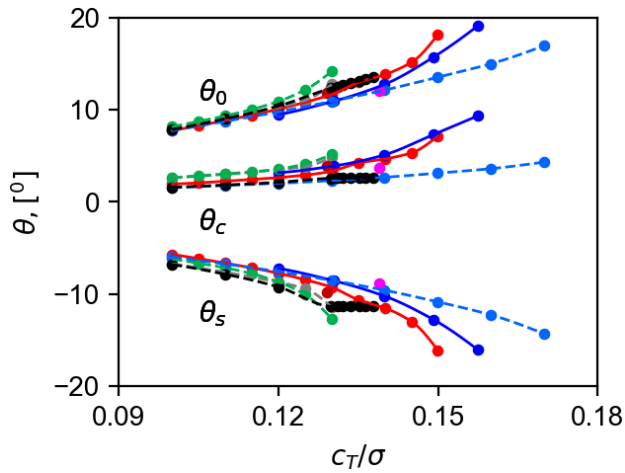

Figure 28: Control angles of the high load condition.

Considering the data plotted in Figure 29, where the required power over thrust is plotted, a similar tendency as for the control angles is observed. For the lower thrust, a good agreement among the partners is found, while for higher thrust the results depart from each other.
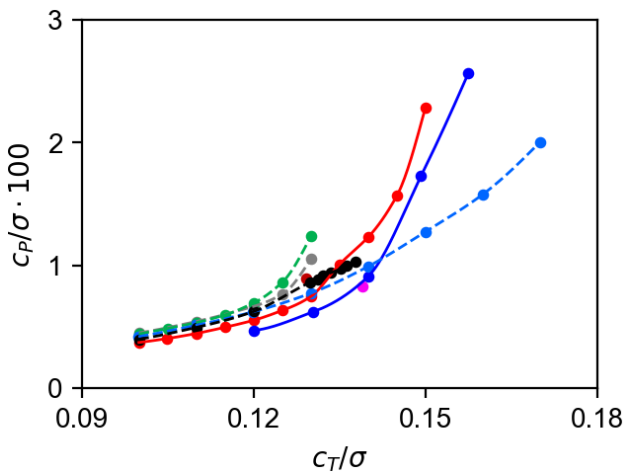

Figure 29: Power required, high load condition.

DLR-CA, DLR-CFD, KU-CA and the JAXA-CFD results start out with a linear trend that then curves upwards as the stall onsets. However, the point at which this occurs is different for all of them. It is noteworthy that the ONERA results remain on a path of gradual increase until they are unable to trim the system anymore.

The vibration intrusion index, VI, is plotted as a function of thrust in Figure 30. This metric shows even less agreement among the partners than the previous metrics and seems to be at very different levels. A commonality observed for DLR-CA, DLR-CFD, KU-CA and JAXA-CFD is that with the onset of the stall (where the power consumption also increases), the vibration index rises. Additionally, for $C_T/\sigma = 0.13$, the CFD-based results arrive at a similar level, which may be coincidental given the otherwise very different behaviour.
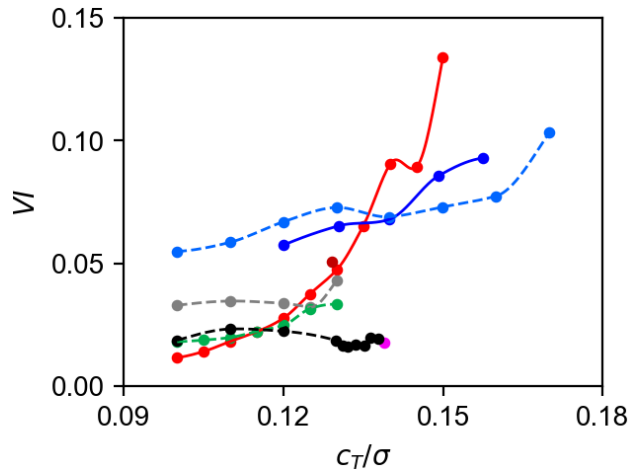

Figure 30: Vibration intrusion index.

To analyze this matter in more detail, the sectional normal force and pitching moment are investigated for the spanwise section at $r/R = 0.67$ in Figures 31 and 32. This spanwise location will be the next closest instrumented section in the experiment to where the vortex of the previous blade passes on the retreating side. For the normal force in Figure 31, a general 2p trend is captured, yet the higher harmonic content caused by advancing and retreating side BVI is differently resolved by the partners. The US-CA result does not capture any of it, whereas DLR-CFD has the most.

The pitching moment in Figure 32 is very similar among the partners for the most part, but in the retreating to aft side of the rotor disc, the results show a noticeable spread. DLR-CFD shows a strong pitching moment stall, with moderate stalls reported by

DLR-CA, KU-CA and JAXA-CFD, but only a mild stall is observed for KARI-CFD, US-CA and ONERA-CA.
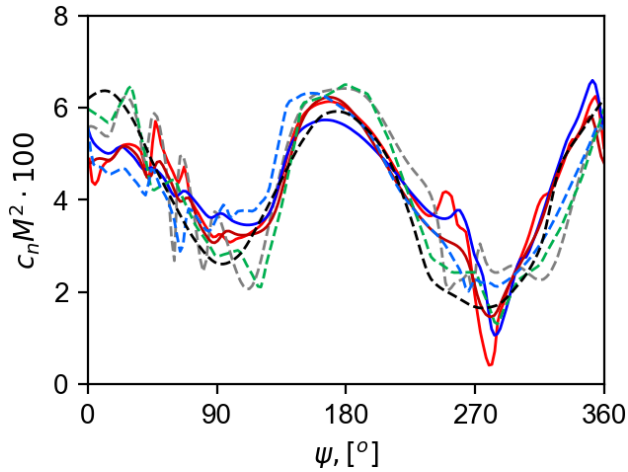

Figure 31: Section normal load coefficient, $r/R = 0.67$, $C_T/\sigma = 0.13$.
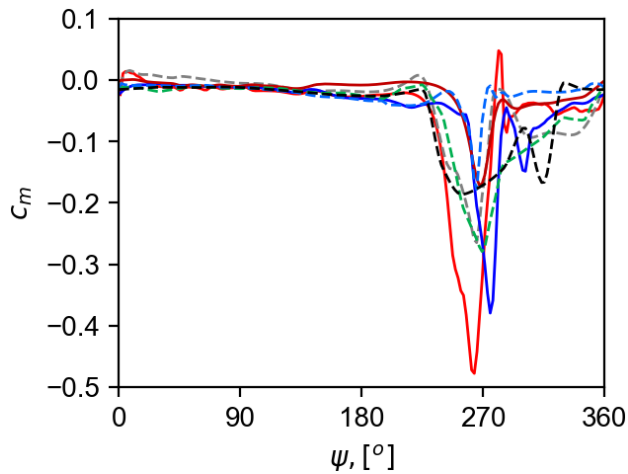

Figure 32: Section moment coefficient, $r/R = 0.67$, $C_T/\sigma = 0.13$.

The pitching moment is linked with the torsional deflection shown in Figure 33. It is seen, that if a severe stall is found in Figure 32, a stronger excitation of the first torsion mode is found here as well. For DLR-CA, the peak-to-peak value of 2.7° is largest, while JAXA-CFD with 1.1° is predicting the lowest range of torsion.

An additional concern of this test case is the blade flapping shown in Figure 34, which remains in acceptable ranges and therefore will likely not be an issue during testing.

The intermediate conclusion from the first phase study of this case is that the ability to predict dynamic stall is a challenging task and likely requires a lot more resources to correctly predict. Some faith is laid into the CFD-based results due to their significantly

higher resolution compared to CA codes. While for DLR-CFD the stall occurs already at lower thrust levels, the severity of stall becomes similar at higher thrust levels for JAXA-CFD. Therefore, it is believed that in the experiment, the exact thrust needs to be found.
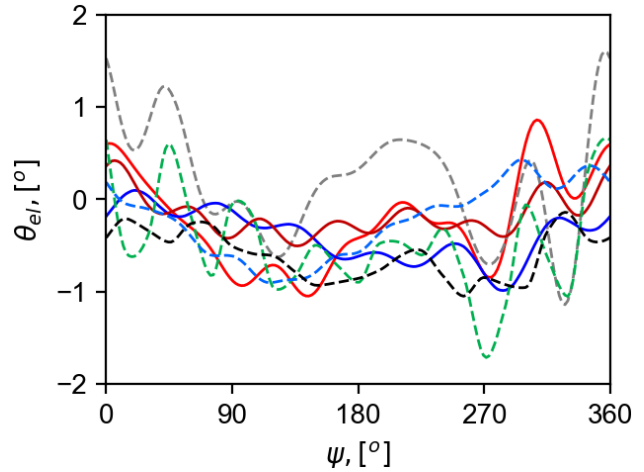

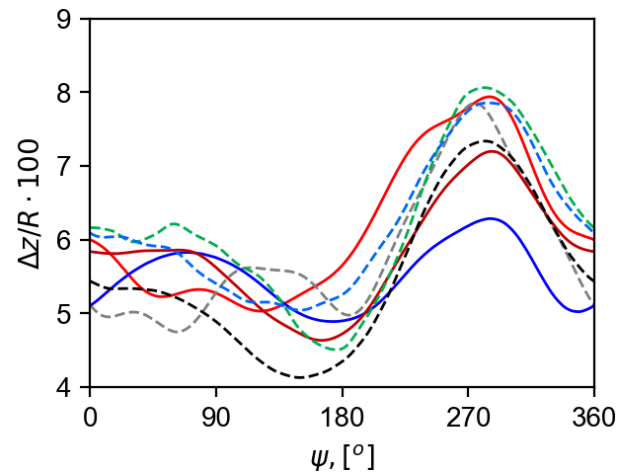Figure 33: Blade tip torsion, $C_T/\sigma = 0.13$.

Figure 34: Vertical blade tip deflection, $C_T/\sigma = 0.13$.

To test the actuation in the second phase of the high load predictions, a data point is sought that shows dynamic stall, but is sufficiently far away from the maximum thrust to avoid undesirable effects when actuating. Because the results have been so different for the partners, the following logic has been applied: A reduction of $\Delta c_T/\sigma = 0.005$ is to be applied to the maximum thrust obtained by the individual partner, or a $C_T/\sigma = 0.13$ is to be applied, whichever number results in a smaller thrust. This allows for trimmable results, while capping at $C_T/\sigma = 0.13$ to ensure that the results do not become too diverse.

At the time of this writing, the predictions were still in progress; thus, not every partner was able to produce

results for this phase. While a wide range of actuations has been investigated, from a steady 0p to 1p and 4p actuations, only the 2p results are presented here for brevity as they delivered the most promising outcome.

In Figures 35 and 36, the required power and vibration intrusion index relative to the baseline value by the respective partners' results are plotted. Despite the attempt to norm the results, the solutions are quite diverse. Nevertheless, a crude observation can be made: using an aft-disc phase ($\phi \approx 330° - 60°$) reduces the required power for all partners, but the required power increases around the front-disc phases ($\phi \approx 90° - 270°$).
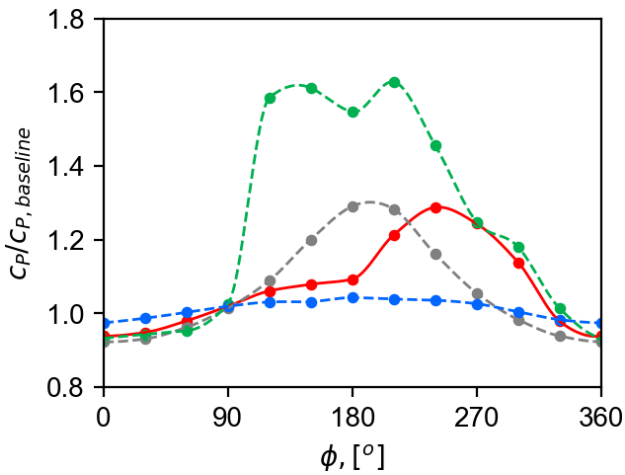

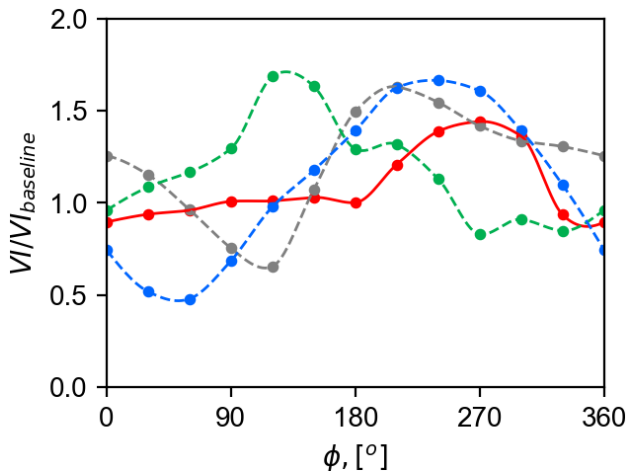Figure 35: Relative power required, $C_T/\sigma = 0.13$, 2p phase sweep.

Figure 36: Vibration intrusion index, $C_T/\sigma = 0.13$, 2p phase sweep.

Looking towards the Vibration Intrusion Index results, they are more diverse than has already been shown for the baseline cases. Here it seems that most, but not all partners, predict an improvement for phases

$\phi \approx 30° - 120°$ and a deterioration for the retreating side phases $\phi \approx 180° - 330°$.

The current working assumption for the second prediction stage of this high load investigation is that a phase of $\phi = 0° - 90°$ at 2p will likely enable benefits in this flight condition and is worth considering in the wind tunnel experiment.

8. HIGH ADVANCE RATIO: L/D RATIO, VIBRATION

The last test matrix scenario considered is a slowed rotor, high advance ratio (HA) flight. The rotor speed is reduced to 50% RPM at the wind speed of 76 m/s, resulting in an advance ratio of $\mu = 0.7$. The 50% reduction is chosen considering the previous slowed rotor test cases such as a full-scale UH-60A rotor[71] and CarterCopter gyroplane test[72]. The present HA condition simulates a high-speed compound helicopter or autogiro configuration of a rotor. The RPM reduction leads to a large increase in the reversed flow region. Trimming the rotor to zero rolling moment results in a significant region of negative lift on the advancing blade tip. This negative lift region results in a high differential aerodynamic loading over the advancing side of the rotor disk. The slowed rotor also drives a large blade flapping due to the decreased centrifugal action and lower loads acting over the blade. Furthermore, the blade natural modes upshift to higher frequency zones (e.g. the first torsion mode shifts from 3.78p to 6.97p). All these features make the HA condition quite challenging from both the aerodynamic and aeroelastic viewpoints.

The goals of the current HA task are set to confirm: first, the prediction capability in capturing the essential aeromechanics phenomena of the slowed rotor (HA1) and second, the benefits in association with the hub vibration and performance aspect exploiting the active twist authority (HA2). The HA1 condition is an unactuated slowed rotor test that has been studied previously in the literature[71],[72] while the HA2 case is unique in this work. It is noted that the STAR HA condition utilizes a limited set of test points, as compared with the wide coverage of test matrix in the UH-60A test campaign[71]. For instance, the collective angle and rotor RPM are kept constant with shaft angles varied from -4° to +4° in the STAR HA condition, whereas in the UH-60A slowed rotor test, both the collective (-0.1° to +8°) and rotor RPM (65%, 40%) are varied as a function of shaft angles (0°, +4°). This reduced test set is used to focus on special features

of the slowed rotor while exploiting the twist actuation gains, under the strict budget and time constraints.

In the HA1 case, a trim to zero hub moments is used to determine the cyclic control angles with the collective pitch fixed at $\Theta_0 = 4°$. Figure 37 shows the comparison of predicted trim control angles with shaft angle variations. An apparent linear response of the trim control angles with shaft angle changes is predicted reasonably among the different approaches, with slight deviations in amplitudes (less than 1°). The calculated thrust values (C_T/σ) indicate a monotonic increase with shaft angles (not shown), as observed in the UH-60A slowed rotor test[71]. This close correlation among the predicted results assures the consistency of the analysis methods with confidence in the trim convergence set for the HA condition.
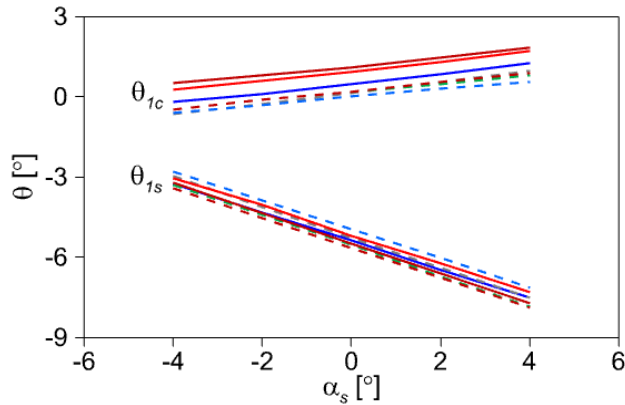

Figure 37: Comparison of trim control angles with shaft angle changes.

Figure 38 illustrates the comparison of results obtained for section normal force coefficients in the time domain, at the radial station of $r/R = 0.875$ with a shaft angle of $\alpha_S = 0°$. Good agreements appear to be obtained in terms of the waveform and peak-to-peak magnitudes among the diverse set of signals that include CSD alone (dashed lines) and CFD/CSD coupled (continuous lines) results.

In general, CFD/CSD predictions indicate larger negative peaks around 90° azimuth angles and more oscillatory signals (i.e. indication of BVI events) in the first and fourth quadrants of the disk than those by CSD alone methods. It is observed that the dominant phase response of the section airloads signal is predicted almost the same by all methods. The large negative peak in the outboard region of the advancing side is expected as the reversed flow regime occupies a substantial portion of the opposite side at $\mu = 0.7$, which leads to high differential airloading over the advancing blades. This has also been confirmed

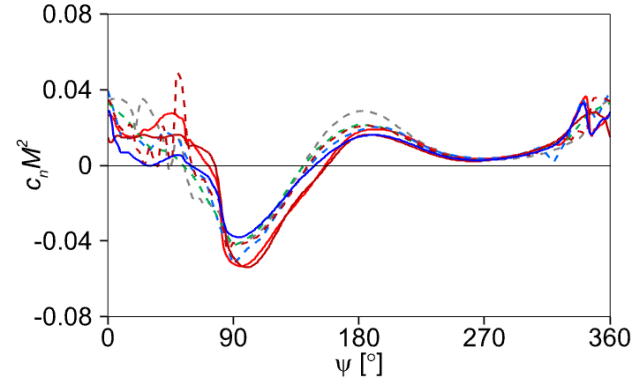considering the contour plots for the section normal forces (not shown).

Figure 38: Comparison of section normal force coefficients at $r/R = 0.875$ ($\alpha_S = 0°$).

Figure 39 shows the comparison of elastic twist deformation at the blade tip when $\alpha_S = 0°$. Though the local response shows substantial scatter among the results, the general trend (nose-down in the advancing side and nose-up in the retreating side) is captured reasonably by the analyses. As can be seen, a highly oscillatory pattern close to 7p is obtained, particularly in CFD/CSD predictions.
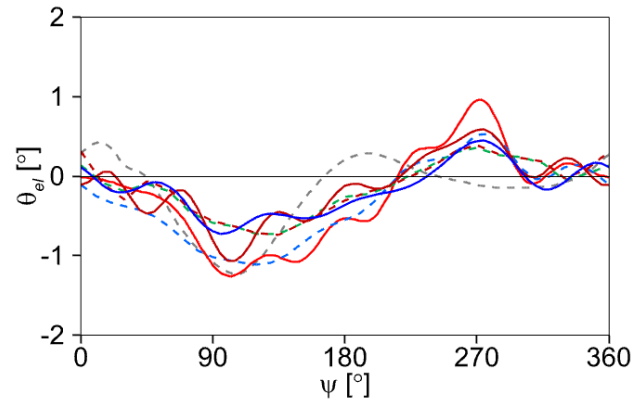

Figure 39: Comparison of tip elastic twist deformation ($\alpha_S = 0°$).

The prominent 7p signal is essentially augmented by the first torsion blade natural frequency shifted by the reduced RPM and is responsible for generating the differential air loading pattern found in the section normal forces (Figure 38) through the mechanism of the trim. It is seen that most CSD predictions except DLR-CA capture the low-frequency waveform of CFD/CSD results while showing some of 7p oscillatory behaviour.

Figure 40 presents the influence of shaft angles on section airloads ($C_n M^2$, $C_m M^2$) and blade elastic deformations (z, θ_{el}). For relative comparison, the mean

values of all predicted results are averaged and presented in% values, with the reference set at the mean of 0° shaft angles (x_0). It is indicated that both, section normal force coefficients and tip flap deflections, increase with shaft angle changes while the mean of either section pitching moments or tip elastic twist deformation remains nearly unchanged. This outcome is consistent with the predicted thrust trends though not shown explicitly.
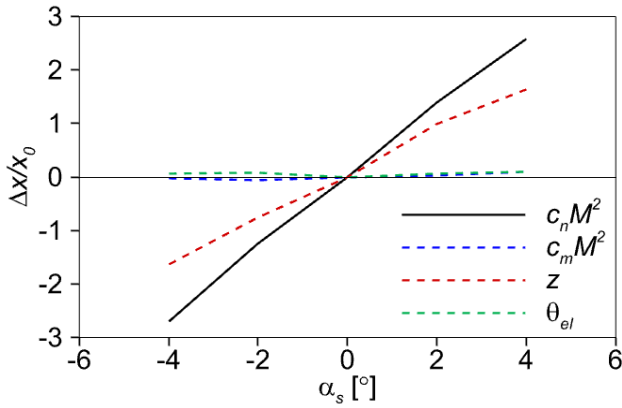

Figure 40: Effect of shaft angles on section airloads and blade deformation (reference value at $\alpha_S = 0°$).

The predicted rotor power (induced plus profile power) is shown in Figure 41 versus α_S changes. As discussed above (Figure 37), the required power in HA condition is expected to be very small due to the trim setup, which may fall within the measurement error of the wind tunnel test capacity (190 kW). Nevertheless, all the predicted results pick up the general up-down trends as shaft angle changes, with upper bounds by KARI-CFD results. The reason for overprediction in KARI-CFD is likely due to its consideration of a blade inboard shank model that has been neglected by other analyses.
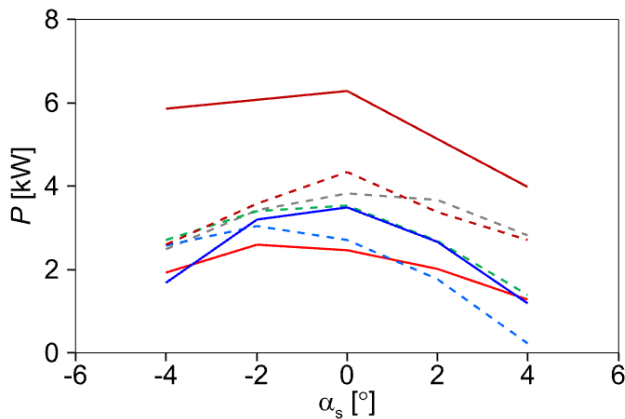

Figure 41: Effect of shaft angles on rotor power.

Figure 42 shows the comparison of equivalent lift-to-drag ratios (L/D_e) with respect to shaft angles. The general trends in L/D_e with shaft angles are captured by the analyses but with wide scatter in amplitudes. The upper and lower bound results are obtained by DLR-CA and KARI-CFD, respectively. The shank model incorporated in the KARI-CFD analysis apparently contributes to underestimate L/D_e predictions relative to the others.
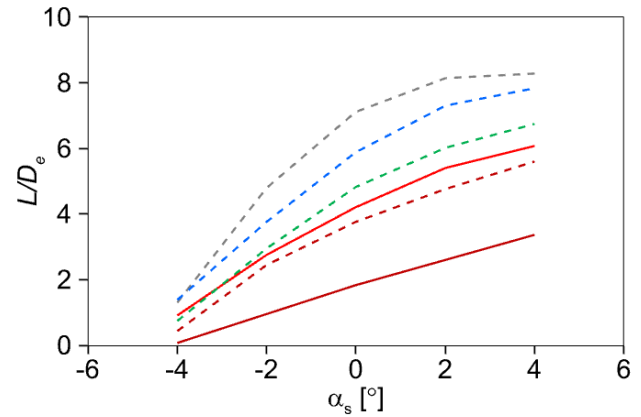

Figure 42: Effect of shaft angles on rotor L/D_e.

Next, the actuation scenarios (HA2) for the minimum vibration and/or the best performance are sought through the application of active twist control. Retrim to the thrust values and hub moments of the corresponding non-actuated cases with the shaft axis fixed at $\alpha_S = 0°$ is applied to examine the active twist gains. The actuation cases include steady voltage and dynamic frequency sweeps with the variations in actuation voltages (amplitudes) and phase angles.

Figure 43 shows the effect of applying steady 0p voltages (U_0) on the vibration intrusion index (VI) defined in Eq. (2), for the rotor in high-μ flight. The actuation voltages are varied from $U_0 = -500$ V to 800 V with an offset of 400 V. Only the predicted results with CA methods are presented in the comparison. It is indicated that most results estimate increased vibration reductions with higher voltages, with maximum gains obtained at 800 V. Up to 38% reduction referenced to the baseline cases is shown with the steady actuation.

The voltage sweep behaviour is also studied for rotor power and L/D_e. It is observed that most predicted results indicate increases in L/D_e at or over 250 V while no significant changes in rotor power are found among the predictions. The increased gains in L/D_e are up to 2.7% (not shown). The favorable zones with possible improvements in L/D_e are indicated in

Figure 43 in the yellow box. In summary, both the vibration reduction and performance (L/D_e) improvement are feasible with active twist control technologies, without incurring significant power penalty.
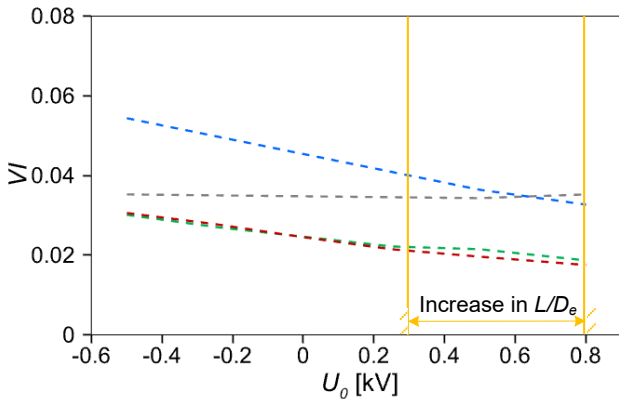

Figure 43: Effect of voltage sweep on VI at steady 0p actuation and 400 V offset.

A 2p actuation is investigated also for performance and vibration behavior of the rotor in high μ flight. Figure 44 shows the phase sweep response of the group simulation results on VI at the dynamic voltage of $U_2 = 500$ V and with 400 V offset. It is observed that the phase sweep has a great potential in reducing hub vibrations, with substantial deviations among the predicted results. Most predictions (KU, KARI, and ONERA) show almost the same waveform in the phase response, with apparent offset by ONERA results.
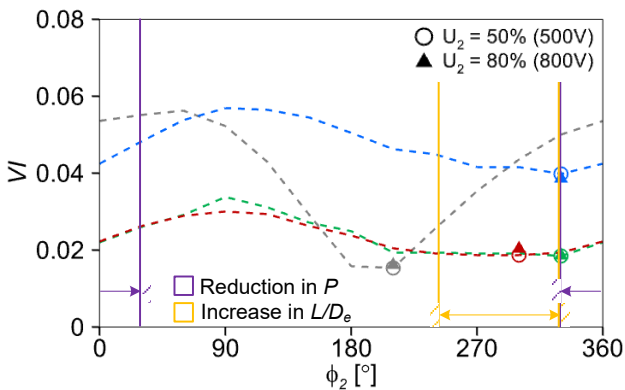

Figure 44: Effect of phase sweep on VI at dynamic 2p actuation ($U_2 = 500$ V) and 400 V offset.

The hollow circles in Figure 44 indicate the best phase angles that could result in a minimum hub vibration. The maximum gain is estimated by DLR-CA, with the percentage values of about 55% based on the unactuated case. It is observed that the phase angle of 330° appears to be one of the best conditions for minimum VI at 2p frequency input. Another

attempt is made to see whether an increase in voltage levels to 800 V can contribute further to reduce the hub vibration, based on the predicted minimum VI locations at 500 V input.

The solid triangles in Figure 44 denote the results with 800 V actuation. Most results (except ONERA) indicate an increase in VI with the increased voltages. This signifies that the vibration reduction gain is non-linear in response to the voltage input. It is concluded that a 500 V input is recommended as the best scenario for the active twist input in a high μ condition.

In Figure 44, the predicted zones of possible improvements in L/D_e and reductions in rotor power are indicated in yellow and purple color, respectively. The maximum gains are predicted to be: 2.9% reduction in rotor power and 2.0% improvement in L/D_e. Though the performance gain is limited (less than 3%), it is likely to meet the best actuation condition, by concurrently reducing VI and improving L/D_e with decreases in required rotor power, when the phase angle is set at 330° with 2p, 500 V active twist input.

9. CONCLUSIONS

The predictions show that:

- The achievable improvement of hover Figure of Merit is rather small, because the available steady active twist of approximately 2° is much smaller than needed.

- In low-speed descent, the BVI noise and vibration reduction by active twist is comparable to that obtained by HHC or IBC.

- In high-speed flight, the power gains due to active twist are comparable to those obtainable by IBC.

- The numerical prediction of the vortex-induced (deep) stall condition at high load is very challenging. Good potential to either reduce the required power or the vibration are foreseen, but results vary due to noticeable differences in the predictions. A reduction of the RPM to 50% of the nominal RPM will likely enable safe operations in the wind tunnel.

- The predictions at high μ with reduced RPM indicated reasonable agreements among the group simulation results. Both steady 0p and dynamic 2p actuation showed significant vibration reduction gains relative to unactuated cases. The amplitude or phase sweep study revealed that the best actuation condition could be met at 2p and 500 V input

with 330° phase angle, for concurrent reduction in hub vibration and rotor power while improving rotor L/D_e.

- The large variety of codes applied are not always agreeing in trends of the results and the analysis of the reasons is part of the future work.

- Despite this, the predictions give very valuable information to the test team for setting up the test matrix to focus on the most promising conditions and make the best use of the available wind tunnel time.

REFERENCES

AHS = American Helicopter Society
ERF = European Rotorcraft Forum
VFS = Vertical Flight Society

[1] Gessow, A., and Myers, G.C.: *Aerodynamics of the Helicopter*, Macmillan, New York, 1952

[2] Johnson, W.: *Helicopter Theory*, Princeton University Press, New Jersey, 1980

[3] Leishman, J.G.: *Principles of Helicopter Aerodynamics*, Cambridge University Press, New York, 2000

[4] Kessler, C.: Active Rotor Control for Helicopters: Motivation and Survey on Higher Harmonic Control, *CEAS Aeronautical Journal*, Vol. 1, (1–4): 3–22, 2011

[5] Kessler, C.: Active Rotor Control for Helicopters: Individual Blade Control and Swashplateless Rotor Designs. *CEAS Aeronautical Journal*, Vol. 1, (1–4): 23–54, 2011

[6] Küfmann, P., Bartels, R., van der Wall, B.G., Schneider, O., Holthusen, H., and Gomes, J.: The First Wind Tunnel Test of the DLR's Multiple Swashplate System: Test Procedure and Preliminary Results, *Journal of the AHS*, Vol. 62, (4): 042002–1–13, 2017

[7] Küfmann, P.M., Bartels, R., van der Wall, B.G., Schneider, O., Holthusen, H., and Postma, J.: The Second Wind–Tunnel Test of DLR's Multiple Swashplate System – IBC on a Five-Bladed Rotor with Fuselage–Mounted (Fixed Frame) Actuators, *CEAS Aeronautical Journal*, Vol. 10, (2): 385–402, 2019

[8] Loewy, R.G.: Recent Developments in Smart Structures with Aeronautical Applications, *Smart Materials and Structures*, Vol. 6, (5): R11–R42, 1997

[9] Chopra, I.: *Recent Progress on the Development of a Smart Rotor System*, 26th ERF, The Hague, Netherlands, Sept. 26–29, 2000

[10] Chopra, I.: Status of Application of Smart Structures Technology to Rotorcraft Systems, *Journal of the AHS*, Vol. 45, (4): 228–252, 2000

[11] Chopra, I.: Review of State of Art of Smart Structures and Integrated Systems, *AIAA Journal*, Vol. 40, (11): 2145–2187, 2002

[12] Thakkar, D., and Ganguli, R.: Active Twist Control of Smart Helicopter Rotor – A Survey, *Journal of Aerospace Sciences and Technologies*, Vol. 57, (4): 429–448, 2005

[13] Friedmann, P.P.: On–Blade Control of Rotor Vibration, Noise, and Performance: Just Around the Corner? The 33rd Alexander Nikolsky Honorary Lecture, *Journal of the AHS*, Vol. 59, (4): 041001–1–37, 2014

[14] Wilkie, W.K., Wilbur, M.L., Mirick, P.H., Cesnik, C.E.S., and Shin, S.J.: *Aeroelastic Analysis of the NASA/Army/MIT Active Twist Rotor*, AHS 55th Annual Forum, Montréal, Canada, May 25–27, 1999

[15] Cesnik, C.E.S., Shin, S.J., Wilkie, W.K., Wilbur, M.L., and Mirick, P.H.: *Modeling, Design, and Testing of the NASA/Army/MIT Active Twist Rotor Prototype Blade*, AHS 55th Annual Forum, Montréal, Canada, May 25–27, 1999

[16] Wilbur, M.L., Yeager, Jr., W.T., Wilkie, W.K., Cesnik, C.E.S., and Shin, S.J.: *Hover Testing of the NASA/Army/MIT Active Twist Rotor Prototype Blade*, AHS 56th Annual Forum, Virginia Beach, VA, May 2–4, 2000

[17] Wilbur, M.L., Mirick, P.H., Yeager, Jr., W.T., Langston, C.W., Cesnik, C.E.S., and Shin, S.J.: Vibratory Loads Reduction Testing of the NASA/Army/MIT Active Twist Rotor, *Journal of the AHS*, Vol. 47, (2): 123–133, 2002

[18] Wilbur, M.L., Yeager, Jr., W.T., and Sekula, M.K.: *Further Examination of the Vibratory Loads Reduction Results from the NASA/Army/MIT Active Twist Rotor Test*, AHS 58th Annual Forum, Montréal, Canada, June 11–13, 2002

[19] Shin, S.J., Cesnik, C.E.S., and Hall, S.R.: *Closed-Loop Control Test of the NASA/Army/MIT Active Twist Rotor for Vibration Reduction*, AHS 59th Annual Forum, Phoenix, AZ, May 6–8, 2003

[20] Bernhard, A.P.F., and Wong, J.: Wind-Tunnel Evaluation of a Sikorsky Active Rotor Controller Implemented on the NASA/Army/MIT Active Twist Rotor, *Journal of the AHS*, Vol. 50, (1): 65–81, 2005

[21] Shin, S.J., Cesnik, C.E.S., and Hall, S.R.: Closed-Loop Control Test of the NASA/Army/MIT Active Twist Rotor for Vibration Reduction, *Journal of the AHS*, Vol. 50, (2): 178–194, 2005

[22] Büter, A., and Breitbach, E.: Adaptive Blade Twist – Calculations and Experimental Results, *Aerospace Science and Technology*, Vol. 4, (5): 309–319, 2000

[23] Wierach, P., Riemenschneider, J., Opitz, S., and Hoffmann, F.: *Experimental Investigation of an Active Twist Model Rotor Blade under Centrifugal Loads*, 33rd ERF, Kazan, Russia, Sept. 11–13, 2007

[24] Wierach, P., Riemenschneider, J., Opitz, S., and Hoffmann, F.: Experimental Investigation of an Active Twist Model Rotor Blade Under Centrifugal Loads, Chapter 32: 391–407 in: Wiedemann, and Sinapius (Eds.): *Research Topics in Aerospace: Adaptive, Tolerant and Efficient Composite Structures*, pp. 391–407, Springer: Berlin-Heidelberg, Germany, 2013

[25] Riemenschneider, J., Keimer, R., and Kalow, S.: *Experimental Bench Testing of an Active-Twist Rotor*, 39th ERF, Moscow, Russia, Sept. 3–5, 2013

[26] Hoffmann, F., Schneider, O., van der Wall, B.G., Keimer, R., Kalow, S., Bauknecht, A., Ewers, B., Pengel, K., and Feenstra, G.: *STAR Hovering Test – Proof of Functionality and Representative Results –,* 40th ERF, Southampton, UK, Sept. 2–4, 2014

[27] Lim, J.W., Boyd, Jr., D.D., Hoffmann, F., van der Wall, B.G., Kim, D.–H., Jung, S.N., Tanabe, Y., Bailly, J., Lienard, C., and Delrieux, Y.: *Aeromechanical Evaluation of Smart–Twisting Active Rotor,* 40th ERF, Southampton, UK, Sept. 2–4, 2014

[28] Bauknecht, A., Ewers, B., Schneider, O., and Raffel, M.: *Aerodynamic Results from the STAR Hover Test: An Examination of Active Twist Actuation*, 41st ERF, Munich, Germany, Sept. 1–3, 2015

[29] Hoffmann, F., Keimer, R., and Riemenschneider, J.: Structural Modeling and Validation of an Active Twist Model Rotor Blade, *CEAS Aeronautical Journal*, Vol. 7, (1): 43–55, 2016

[30] Kalow, S., van de Kamp, B., Keimer, R., and Riemenschneider, J.: *Experimental Investigation and Validation of Structural Properties of a New Design for Active Twist Rotor Blades*, 43rd ERF, Milan, Italy, Sept. 12–15, 2017

[31] Kalow, S., van de Kamp, B., Balzarek, C., and Riemenschneider, J.: *Manufacturing of a Next Generation Active Twist Helicopter Rotor Blade and Experimental Results of Functionality Test*, AHS 74th Annual Forum, Phoenix, Arizona, May 14–17, 2018

[32] Kalow, S., van de Kamp, B., Keimer, R., and Riemenschneider, J.: *Next Generation Active Twist Helicopter Rotor Blade – Simulated Results Validated by Experimental Investigation*, 45th ERF, Warsaw, Poland, Sept. 17–20, 2019

[33] Crews, S.T., and Hamilton, B.W., Army Helicopter Crew Seat Vibration – Past Performance, Future Requirements, AHS North East Region National Specialists' Meeting on Helicopter Vibration, Hartford, CT, Nov. 2–4, 1981

[34] van der Wall, B.G.: Analytic Formulation of Unsteady Profile Aerodynamics and its Application to Simulation of Rotors, ESA–TT–1244, 1992 (Translation of the Research Report DLR–FB 90–28, 1990)

[35] van der Wall, B.G., Lim, J.W., Smith, M.J., Jung, S.N., Bailly, J., Baeder, J.D., and Boyd, D.D.: The HART II International Workshop: An Assessment of the State–of–the–Art in Comprehensive Code Prediction, *CEAS Aeronautical Journal*, Vol. 4, (3): 223–252, 2013

[36] Houbolt, J.C., and Brooks, G.W.: *Differential Equations of Motion for Combined Flapwise Bending, Chordwise Bending, and Torsion of Twisted Nonuniform Rotor Blades*, NACA TN 3905, 1957

[37] Leiss, U.: *A Consistent Mathematical Model to Simulate Steady and Unsteady Rotor–Blade Aerodynamics*, 10th ERF, The Hague, Netherlands, Aug. 28–31, 1984

[38] Mangler, K.W., and Squire, H.B.: *The Induced Velocity Field of a Rotor*, ARC R&M 2642, 1950

[39] Beddoes, T.S.: *A Wake Model for High Resolution Airloads*, AHS/ARO 1st International Conference on Rotorcraft Basic Research, Research Triangle Park, North Carolina, Feb. 19–21, 1985

[40] Yin, J., and Delfs, J.: *Improvement of DLR Rotor Aero–Acoustic Code (APSIM) and its Validation with Analytic Solution*, 29th ERF, Friedrichshafen, Germany, Sept. 16–18, 2003

[41] Farassat, F.: Derivation of Formulation 1 and 1A of Farassat, NASA TM–2007–214853, 2007

[42] Raddatz, J., and Fassbender, J.K.: Block Structured Navier–Stokes Solver FLOWer, in: Kroll and Fassbender (Eds): *Notes on Numerical Fluid Mechanics and Multidisciplinary Design: MEGAFLOW – Numerical Flow Simulation for Aircraft Design*, Vol. 89: 27–44, Springer: Berlin–Heidelberg, Germany, 2005

[43] Benoit, B., Dequin, A.M., Kampa, K., von Grünhagen, W., Basset, P.M., and Gimonet, B.: *HOST, a General Helicopter Simulation Tool for Germany and France*, AHS 56th Annual Forum, Virginia Beach, VA, May 2–4, 2000

[44] Potsdam, M., Yeo, H., and Johnson, W.: *Rotor Airloads Prediction Using Loose Aerodynamic/Structural Coupling*, AHS 60th Annual Forum, Baltimore, MD, June 7–10, 2004

[45] Wilke, G.: Comparisons of Different Spatial Schemes and Limiters for Helicopter Flows, in: Dillmann et al. (Eds): *Notes on Numerical Fluid Mechanics and Multidisciplinary Design: New Results in Numerical and Experimental Fluid Mechanics XIII: Contributions of the 22nd STAB/DGLR Symposium*, Vol. 151: 418–427, Springer: Berlin–Heidelberg, Germany, 2021

[46] Shur, M.L., Spalart, P.R., Strelets, M.K., and Travin, A.K.: A Hybrid RANS–LES Approach with Delayed–ES and Wall–Modelled LES Capabilities, *International Journal of Heat and Fluid Flow*, Vol. 29, (6): 1638–1649, 2008

[47] Dacles–Mariani, J., Kwak, D., and Zilliac, G.: On Numerical Errors and Turbulence Modeling in Tip Vortex Flow Prediction, *International Journal for Numerical Methods in Fluids*, Vol. 30, (1): 65–82, 1999

[48] Heister, C.C.: A Method for Approximate Prediction of Laminar–Turbulent Transition on Helicopter Rotors, *Journal of the AHS*, Vol. 63, (3): 1–14, 2018

[49] Basset, P.M., Heuze, O., Prasad, J. V. R., and Hamers, M.: *Finite State Rotor Induced Flow Model for Interferences and Ground Effect*, AHS 57th Annual Forum, Washington DC, May 9–11, 2001

[50] Arnaud, G., and Beaumier, P.: *Validation of R85/METAR on the Puma RAE Flight Tests*, 18th ERF, Avignon, France, Sept. 15–18, 1992

[51] Rodriguez, B.: *Blade Vortex Interaction and Vortex Ring State Captured by a Fully Time Marching Unsteady Wake Model Coupled with a Comprehensive Dynamics Code*, Heli Japan, Saitama, Japan, Nov. 1–3, 2010

[52] Michéa, B., Desopper, A., and Costes, M.: *Aerodynamic Rotor Loads Prediction Method with Free–Wake for Low Speed Descent Flight*, 18th ERF, Avignon, France, Sept. 15–18, 1992

[53] Rahier, G., and Delrieux, Y.: *Improvement of Helicopter Rotor Blade–Vortex Interaction Noise Prediction Using a Rotor Wake Roll–Up Model*, 1st Joint CEAS/AIAA Aeroacoustics Conference (16th AIAA Aeroacoustics Conference), Munich, Germany, June 12–15, 1995

[54] Spiegel, P., Rahier, G., and Michéa, B.: *Blade Vortex Interaction Noise: Prediction and Comparison with Flight and Wind Tunnel Tests*, 18th ERF, Avignon, France, Sept. 15–18, 1992

[55] Spiegel, P., and Rahier, G.: *Theoretical Study and Prediction of BVI Noise Including Close Interactions*, AHS Technical Specialists Meeting on Rotorcraft Acoustics and Fluid Mechanics, Valley Forge, Philadelphia, PA, Oct. 15–17, 1991

[56] Johnson, W.*: Rotorcraft Aerodynamic Models for a Comprehensive Analysis*, AHS 54th Annual Forum, Washington, DC, May 20–22, 1998

[57] Lopes, L., and Burley, C.L.: *Design of the Next Generation Aircraft Noise Prediction Program: ANOPP2*, 17th AIAA/CEAS Aeroacoustics Conference (32nd AIAA Aeroacoustics Conference), Paper AIAA 2011–2854, Portland, OR, June 5–8, 2011

[58] Lee, H., Yu, D., Kwon, O.J., and Kang, H.J.: Numerical Investigation about Aerodynamic Interference of Complete Helicopter Configurations, *International Journal of Aeronautical and Space Sciences*, Vol. 12, (2): 190–199, 2011

[59] Tanabe, Y., Saito, S., and Sugawara, H.: *Construction and Validation of an Analysis Tool Chain for Rotorcraft Active Noise Reduction*, 38th ERF, Amsterdam, Netherlands, Sept. 4–7, 2012

[60] Langtry, R.B., and Menter, F.R.: Correlation–Based Transition Modeling for Unstructured Parallelized Computational Fluid Dynamics Codes, *AIAA Journal*, Vol. 47, (12): 2894–2906, 2009

[61] Steijl, R., Barakos, G.N., and Badcock, K.: A Framework for CFD Analysis of Helicopter Rotors in Hover and Forward Flight, *International Journal for Numerical Methods in Fluids*, Vol. 51, (8): 819–847, 2006

[62] Osher, S., and Chakravarthy, S.: Upwind Schemes and Boundary Conditions with Applications to Euler Equations in General Geometries, *Journal of Computational Physics*, Vol. 50, (3): 447–481, 1983

[63] van Leer, B.: Towards the Ultimate Conservative Difference Scheme. V. A Second–Order Sequel to Godunov's Method, *Journal of Computational Physics*, Vol. 32, (1): 101–136, 1979

[64] van Albada, G.D., van Leer, B., and Roberts, W.W.: A Comparative Study of Computational Methods in Cosmic Gas Dynamics, *Astronomy and Astrophysics*, Vol. 108, (1): 76–84, 1982

[65] Jameson, A.: *Time–Dependent Calculations Using Multigrid, with Applications to Unsteady Flows Past Airfoils and Wings*, AIAA 10th Computational Fluid Dynamics Conference, Honolulu, HI, June 24–26, 1991

[66] Axelsson, O.: *Iterative Solution Methods*, Cambridge University Press: Cambridge, MA, 1994

[67] Menter, F.R.: Two–Equation Eddy–Viscosity Turbulence Models for Engineering Applications, *AIAA Journal*, Vol. 32, (8): 1598–1605, 1994

[68] Dehaeze, F., and Barakos, G.N.: Hovering Rotor Computations Using an Aeroelastic Blade Model, *Aeronautical Journal*, Vol. 116, (1180): 621–649, 2012

[69] Smith, M.J., Gardner, A.D., Jain, R., Peters, D., and Richez, F.: *Rotating Wing Dynamic Stall: State of the Art and Future Directions*, VFS 76th Annual Forum, Virtual, Oct. 6–8, 2020

[70] Castells, C., Richez, F., and Costes, M.: A Numerical Analysis of the Dynamic Stall Mechanisms on a Helicopter Rotor from Light to Deep Stall, *Journal of the AHS*, Vol. 65, (3): 1–17, 2020

[71] Datta, A., Yeo, H., and Norman, T.R.: *Experimental Investigation and Fundamental Understanding of a Slowed UH–60A Rotor at High Advance Ratios*, AHS 66th Annual Forum, Virginia Beach, VA, May 3–5, 2011

[72] Carter, J.: *CarterCopter – A High Technology Gyroplane*, AHS Vertical Lift Design Conference, San Francisco, CA, Jan. 19–21, 2000